



A facile one-pot synthesis of TiO₂-based nanosheets loaded with Mn_xO_y nanoparticles with enhanced visible light-driven photocatalytic performance for removal of Cr(VI) or RhB

Dingze Lu, Pengfei Fang*, Xinzhaio Liu, Shengbin Zhai, Chunhe Li, Xiaona Zhao, Junqian Ding, Ruyue Xiong

Department of Physics and Key Laboratory of Artificial Micro- and Nano-structures of Ministry of Education, Wuhan University, Wuhan 430072, China

ARTICLE INFO

Article history:

Received 17 March 2015

Received in revised form 25 May 2015

Accepted 29 May 2015

Available online 1 June 2015

Keywords:

TiO₂-based nanosheets

Mn_xO_y loaded

Surface enrichment of Mn_xO_y nanoparticles

Photodegradation of rhb

Cr(VI) reduction

ABSTRACT

This paper reports a facile one-pot approach for Mn_xO_y (Mn = Mn²⁺, Mn³⁺) loaded TiO₂-based nanosheets (Mn-TNSs) with surface enrichment of Mn_xO_y nanoparticles via a simple hydrothermal route. The as-synthesized samples showed clearly sheet-like structure, with high specific surface area (200–300 m²/g) and small thickness (ca. 4 nm). The small Mn_xO_y nanoparticles with uniform size (1–2 nm) were highly dispersed on the surface of the TNSs. Loaded Mn_xO_y not only have influenced the crystal structure and surface area of the TNSs, but also resulted in considerable enhancement of visible-light absorption and red-shift for TNSs. The results of X-ray photoelectron spectroscopy showed that Mn²⁺ and Mn³⁺ co-exist in Mn-TNSs. The loading of Mn_xO_y on TNSs resulted in changes in binding energies of Ti and O. The concentration of Ti³⁺ increased gradually with the amount of loaded Mn_xO_y increasing. The photo-reactivity of the samples were evaluated by measuring the formation of photo-induced hydroxyl radical ([•]OH) using coumarin (COU) as a probe molecule and photocatalytic degradation of Rhodamine B (RhB) and dichromate (Cr(VI)) under visible-light irradiation. It has been found that the Mn-TNSs photocatalysts showed better visible-light photocatalytic activity for aqueous RhB or Cr(VI) solution. The photocatalytic activity gradually increased with the content of Mn_xO_y increasing initially, and then decreased after attaining a maximum value at an optimal content (2.5 at.%) of Mn_xO_y in TNSs for degradation of aqueous RhB or Cr(VI) solution, respectively. The cyclic tests that performed five times demonstrated high stability and recyclable usability of the photocatalysts. A possible alternate mechanism for the enhancement of the photocatalytic activity under visible-light irradiation was also proposed.

© 2015 Elsevier B.V. All rights reserved.

1. Introduction

The removal of toxic contaminants from water is a big challenge, especially for wastewater of industrial and municipal fields. Generally, wastewater contains a lot of inorganic and organic pollutants. Most of the inorganic pollutants are toxic heavy metals such as Cr, Pb, Hg and Cd. Due to their toxicity, bioaccumulation and persistence, the presence of these heavy metals became a serious problem in the aquatic environment, while the organic pollutants like Rhodamine B, methyl orange, and phenol in water also have been causing serious environmental problems. The co-existence of metal ions and organic matter in wastewater is a common phenomenon, and the simultaneous removal of these

pollutants from wastewater has particular significance in pollution control and remediation [1–3]. Currently used methods for removing the pollutants from wastewaters include biological, physical and chemical treatments. Among numerous treatments, photocatalytic technology is known as a promising case due to its ability to mineralize most of the organic pollutants by using only luminous energy. TiO₂ has been proved to be the most representative and extensively used photocatalyst, owing to its high photo-activity, low cost, non-toxicity, high oxidation ability, and relatively high chemical stability [4,5]. However, its relatively wide band gap (~3.2 eV) and the high recombination rate of the photo-generated electron-hole pairs hinder its large-scale applications [6,7]. Therefore, considerable efforts have been made to narrow the band gap to shift the absorption edge of TiO₂-based materials deeper into the visible-light region of the electromagnetic spectrum, where the Sun's total irradiance lies nearly 42%.

* Corresponding author. Tel.: +86 27 6875 2003; fax: +86 27 6875 2003.
E-mail address: fangpf@whu.edu.cn (P. Fang).

Further more, the morphology of TiO_2 plays a vital role in photocatalytic activities. As is well known that a larger specific surface area allows photocatalysts to expose to the light effectively as well as make contact with more dye molecules for efficient photocatalytic reaction, and smaller thickness of photocatalyst may be beneficial to improve the separation rate of photo-generated electron–hole pairs. Hence, the manipulation of morphology of TiO_2 -based photocatalysts has attracted attention of many researchers. As a result, TiO_2 has been reported in different morphologies in recent years, e.g., nanofibers, nanotubes, nanorods, nanosheets, and nanoflowers [8–13]. Comparing with other morphologies of TiO_2 -based photocatalysts, nanosheets possess higher specific surface area and smaller thickness. These advantages make nanosheets be expected to exhibit excellent photocatalytic activity. Various methods have been attempted for the preparation of nanosheets so far, such as hydrothermal method, sol–gel method, chemical vapor decomposition (CVD) methods, etc [14–18]. Hydrothermal method is one of the most popular methods due to the advantages of simpleness and convenience. TiO_2 nanoparticles (3D) take the form of nanosheets (2D) and finally nanotubes (1D) under hydrothermal conditions [19]. Controlling the environment of the reaction, results in the synthesis of different nanostructures of TiO_2 -based nanomaterials. Our previous work [20] shows that, TiO_2 -based nanosheets (TNSs) with high specific surface area ($339\text{ m}^2/\text{g}$) can be synthesized. The thickness of single nanosheet has reached to only 4–5 nm. Moreover, UV–vis photocatalytic efficiency of TNSs is better than Degussa P25 when degrading Rhodamine B (RhB), methylene blue (MB), crystal violet (CV), etc [20,21].

However, TNSs also suffer from the same problems with that of other TiO_2 -based photocatalysts, such as high recombination rate of photo-generated electron–hole pairs and low utilization efficiency for the solar energy. To solve these problems, transition metal oxides (M_xO_y) loading is one of the mostly adopted strategies. The loaded transition metal oxides could serve as charge-carrier traps to suppress the recombination of the photo-generated carriers, and they could extend the spectral response of TiO_2 to visible-light range. Pelaez et al. have reported that TiO_2 modified with transition metals (Fe, Cu, Co, Ni, Cr, V, Mn, and Mo) not only showed a shift in absorption edge towards the visible region, but also enhanced photocatalytic activity [22–25]. Devi et al. investigated the photocatalysts modified with transition metals (Fe, Cr, Co, Mn, V, and Ni) by theoretical modeling. It has been showed that Mn among the 3d metals is the most promising in permitting significant optical absorption in the visible light region, through the combined effects of narrowed band gap and the introduction of intermediate bands (IBs) within the forbidden gap [26–28]. Mohamed et al. and Li et al. found that $\text{MnO}_x/\text{TiO}_2$ heterogeneous mixed oxides have exhibited better photocatalytic activity than pure TiO_2 for oxidation of different organic compounds such as, indigo carmine, NO reduction, but it is inferior to Degussa P25 [29,30]. Therefore, it can be inferred that Mn_xO_y -loaded TNSs may be an ideal photocatalytic material with high photocatalytic activity. In addition, for the synthesis of M_xO_y -loaded photocatalysts, some techniques have been reported, such as hydrothermal method, sol–gel method and wet impregnation method [23,31,32]. However, the approaches reported on M_xO_y -loaded photocatalysts are usually multi-step: to introduce M_xO_y nanoparticles on TiO_2 -based photocatalysts, initial preparation of TiO_2 nanomaterials is essential. Especially, single-step synthesis to directly achieve Mn_xO_y -loaded TNSs has never been reported. So it is meaningful to develop a facile alternative single-step method to synthesize the TNSs loaded with highly dispersed Mn_xO_y nanoparticles.

In this work, a facile one-pot hydrothermal synthesis was utilized to prepare TNSs loaded with surface enrichment of Mn_xO_y nanoparticles. The small Mn_xO_y nanoparticles were highly

dispersed on the surface of TNSs, which is crucial to increase the amount of active sites on the surface of photocatalysts. The dichromate (Cr(VI)) was employed as a model of inorganic pollutants since it is one of the most toxic ions in the environment, posing toxicity to most organisms at the concentrations of higher than 0.05 ppm; Rhodamine B, a representative of dyestuff, was selected as the oxidizable organic compound, which may bring about various adverse health and environmental effects. The Mn_xO_y -content-dependent photocatalytic activity was evaluated by the degradation of RhB or Cr(VI) in aqueous solution under visible-light irradiation. An alternative possible mechanism is also proposed for the enhancement of the visible-light photocatalytic activity.

2. Materials and methods

2.1. Preparation of photocatalysts

Degussa P25 (TiO_2 , 80% anatase, 20% rutile) is the product of Degussa Co., Ltd. The NaOH, HNO_3 , acetone ($\text{C}_3\text{H}_6\text{O}$), phosphoric acid (H_3PO_4), 1, 5-Diphenylcarbohydrazide ($\text{C}_{13}\text{H}_{14}\text{N}_4\text{O}$), ethyl alcohol ($\text{C}_2\text{H}_5\text{OH}$), $\text{Mn}(\text{NO}_3)_2$, H_2O_2 , Rhodamine B (RhB), and potassium dichromate ($\text{K}_2\text{Cr}_2\text{O}_7$) were provided by Sinopharm Chemical Reagent Co., Ltd, and coumarin was obtained from Alfa Aesar. All of the reagents were analytically pure grade and used without any further purification. Deionized water was used in all experiments.

In a typical preparation procedure, 0.8 g P25 was dispersed in 50 mL of 10 mol/L NaOH solution under intense stirring. A certain amount of manganese nitrate solution was dropped slowly into the suspension. After magnetically stirred for 1 h, the mixture was treated at 130°C for 3 h in a 100 mL Teflon-lined autoclave. After the reaction, the autoclave was cooled down to the room temperature by water-cooling. The resultant white powders were washed with deionized water until their pH reached 7, and followed by the proton exchange in 200 mL of diluted HCl solution. Finally, the powders were treated with deionized water for several times and then dried at 70°C for 12 h. The obtained samples were denoted by $x\text{-Mn-TNSs}$, where x ($x = 0.5\%, 1.0\%, 1.5\%, 2.0\%, 2.5\%, 3.0\%, 3.5\%$, and 5.0%) represented $\text{Mn}(\text{NO}_3)_2$ concentration in the precursor solution. For comparison, undoped nanosheets (TNSs) were also prepared following the same process without adding any manganese source.

2.2. Characterization of photocatalysts

The morphological features of the specimens were characterized by scanning electron microscopy (SEM) (SIRION, FEI, Netherlands), transmission electron microscopy (TEM) on JEOL TEM-2010 (HT) instrument, and high-resolution transmission electron microscopy (HRTEM) on JEM-2010 FEM. The results of X-ray diffraction (XRD) were collected on Bruker D8 advance X-ray diffractometer by $\text{Cu K}\alpha$ radiation and the accelerating voltage and current were 40 kV and 40 mA, respectively. The results were obtained with a step of 0.02° in the range (2θ) from 20° to 80° . An atomic force microscopy (AFM) was used to examine the surface morphology and thickness of samples. The measurement was carried out in a tapping model, with a driving frequency of 130 kHz at a scan speed of 0.4 Hz using a silicon cantilever with a normal spring constant of 16 N m^{-1} . The specific surface areas (S_{BET}) were measured by obtaining nitrogen adsorption–desorption isotherm at 77 K using the instrument (JW-BK122W, China). Raman spectra were obtained by Horiba Lab RAM HR Raman spectrometer with an excitation wavelength of 448 nm. UV–vis diffuse reflectance spectra (DRS) of the samples were measured using Shimadzu UV-2550 spectrometer equipped with a diffuse reflectance attachment with a BaSO_4 -coated integrating sphere against a BaSO_4

reference. X-ray photoelectron spectroscopy (XPS, Thermo Electron VG Multilab2000) was utilized to analyze the chemical composition of samples and the valence states of various elements. The binding energies were referenced to the C 1s at 284.6 eV. Acq Method was applied by the software of XPS Peak 4.1 and the spectra were analyzed by carrying out a Shirley background subtraction. The fluorescence spectra (FL) were surveyed by a Hitachi FL 4600 using the PMT voltage of 700 V to study the recombination efficiency of photo-generated electrons and holes.

2.3. Measurements of photocatalytic performance

2.3.1. Evaluation of RhB solution

The photocatalytic activities of photocatalysts were evaluated by the degradation of RhB solution. The light source was replaced by a 300 W Xe lamp. The distance of separation between the Xe lamp and the RhB solution is 15 cm. In photocatalytic reaction, the suspensions of the reaction were obtained by adding 0.1 g of photocatalyst into 100 mL of 20 mg/L RhB solution. The reaction apparatus were put into water bath to maintain at ambient temperature. The Xe lamp was turned on after stirring the solution in darkness for 1 h to make sure that the adsorption–desorption equilibrium has been established before the photocatalytic reaction. The whole reaction process lasted for 70 min. Every 10 min, 1.6 mL of solution was collected and centrifuged to separate the photocatalyst at a speed of 1200 r/min for 2 min. The final testing samples were obtained by 0.8 mL of supernatant liquor mixed with 2.4 mL of deionized water. The concentrations of RhB solution were determined by the UV–vis spectrometer. Blank experiment was carried out without photocatalysts to test the stability of RhB molecules. When the visible-light photocatalytic reaction was performed, a cut-off filter ($\lambda \geq 420$ nm) was put on the top of the apparatus of the reaction. The reusability of photocatalyst was checked by repeating at least three times, and it can be found that the error bar was within 5.0%.

2.3.2. Evaluation of dichromate ($K_2Cr_2O_7$) solution

The photocatalytic reduction of aqueous Cr(VI) to Cr(III) was performed 25 °C by a 200 mL quartz reactor containing 100 mg photocatalyst and 100 mL of Cr(VI) aqueous solution at a concentration of 50 ppm. The pH values of reacting solutions were adjusted with HCl or NaOH solution. Without any additives, the pH value of the suspension was found at around 7. Monitoring adsorption in the dark was carried out by periodically withdrawing a small amount of solution (0.2 mL), diluting, complexing and measuring. Once reaching the adsorption–desorption equilibrium, the reactor was exposed to a 300 W Xe lamp. The total duration of the reaction process was 70 min. For every 10 min, 0.8 mL of solution was collected and centrifuged for 2 min to separate the photocatalyst at a speed of 1200 r/min. The final samples were obtained by 0.4 mL of supernatant liquor mixed with 2.8 mL of deionized water. The Cr(VI) content in the supernatant solution was analysed colorimetrically at 540 nm using the diphenylcarbazide method (DPC) by UV–vis spectrometer. When the photocatalytic activity was evaluated under visible-light irradiation, a cut-off filter ($\lambda \geq 420$ nm) was kept on the top of the apparatus.

2.3.3. Evaluation of simultaneous photocatalytic decontamination of Cr(VI) and RhB

Similarly, the co-existence of RhB and Cr(VI) was carried out at 25 °C by a 200 mL quartz reactor containing 100 mg photocatalyst and 100 mL aqueous solution with RhB suspension and Cr(VI) ion concentration being maintained at 20 ppm and 50 ppm, respectively. The pH value of reaction solution was controlled at 1.0 by the addition of HCl solution. The Xe lamp was turned on after stirring in darkness for 1 hour to make sure that the adsorption–desorption

equilibrium has been established before the photocatalytic reaction. The whole reaction process took place for 70 min. The Cr(VI) content in the supernatant solution was measured colorimetrically at 540 nm using the DPC method by UV–vis spectrometer. The concentration of RhB was also determined spectrometrically at 554 nm. A calibration based on Beer–Lambert law was used to quantify the concentration.

2.4. Analysis of photogenerated hydroxyl radicals ($\bullet OH$)

The formation of $\bullet OH$ radicals on the illuminated photocatalysts was analyzed by the photoluminescence (PL) technique using coumarin (COU) as a probe molecule. COU can readily react with $\bullet OH$ to form highly fluorescent COU–OH adducts (7-hydroxycoumarin). The PL intensity of 7-hydroxycoumarin (7-HC) was proportional for the amount of $\bullet OH$ radicals formed on the surface of the photocatalysts. The cut-off filters ($\lambda \geq 420$ nm) were used to obtain visible light. The reaction suspensions were carried out by adding photocatalyst (0.2 g) into aqueous COU solution (1 mM, 100 mL). After being magnetically stirred in dark for an hour to establish an adsorption–desorption equilibrium, the suspensions containing COU as well as photocatalyst powder was irradiated by 300 W Xe lamp and was kept under constant air-equilibrated conditions during the irradiation. At the given time intervals of 5 min, PL spectra of 7-HC product were detected on a fluorescence spectrophotometer (Hitachi F-4600). The increase in the PL intensity at 450 nm of 7-HC by excitation with a wavelength of 342 nm was measured.

3. Results and discussion

3.1. Morphology, microstructure and chemical state of the $Mn_xO_y/TNSs$ photocatalysts

Fig. 1 depicts the SEM and AFM images of P25, TNSs, and 5.0%-Mn-TNSs samples. As shown in Fig. 1a–b, the pristine TiO_2 products have a granular morphology and the granules are nearly mono disperse in size of dozens of nanometers. After hydrothermal treatment at 130 °C for 3 h (Fig. 1c), uniform sheet-like clusters of nanosheets were obtained, which is accordance with the previous reports [21,33]. The formation of TNSs can be ascribed to the exfoliation of granular TiO_2 into sheet-like structure under alkaline hydrothermal conditions. During the reaction, plenty of Ti–O bonds of P25 are broken, causing the split of TiO_2 nanoparticles. As a consequence, the TiO_2 nanoparticles are stripped into smaller planar nanosheets. Finally, these smaller planar nanosheets join together to form larger planar nanosheets. Fig. 1d shows the SEM image of 5.0%-Mn-TNSs. It can be seen that 5.0%-Mn-TNSs have maintained a sheet-like structure. In other words, the nanosheets structure was not destroyed after being introduced manganese during the hydrothermal treatment. In addition, TiO_2 -based nanosheets possess small thickness (ca. 3.6 nm) as shown in Fig. 1f, which are much thinner than that of the raw TiO_2 nanoparticles. The thinness of nanosheets leads to a decrease in the diffusion path of photo-generated carriers, reaching to the surface of nanosheets, which may be beneficial to the enhancement of separation rate of photo-generated electron–hole pairs.

Fig. 2 displays TEM and high-resolution (HR) TEM images of P25, TNSs, 2.5%-Mn-TNSs, and 5.0%-Mn-TNSs. From Degussa P25 (Fig. 2a), granular crystals with diameters of 20–40 nm can be observed. The SAED pattern possesses diffraction lines which indicate the polycrystalline phases, namely, (1 0 1), (0 0 4), (2 0 0), (2 0 4), (2 1 5) diffractions of anatase phase and (2 1 1), (1 1 2) diffractions of rutile phase. However, sheet-like products were found in the samples (Fig. 2c, e, and g) after 3 h of hydrothermal

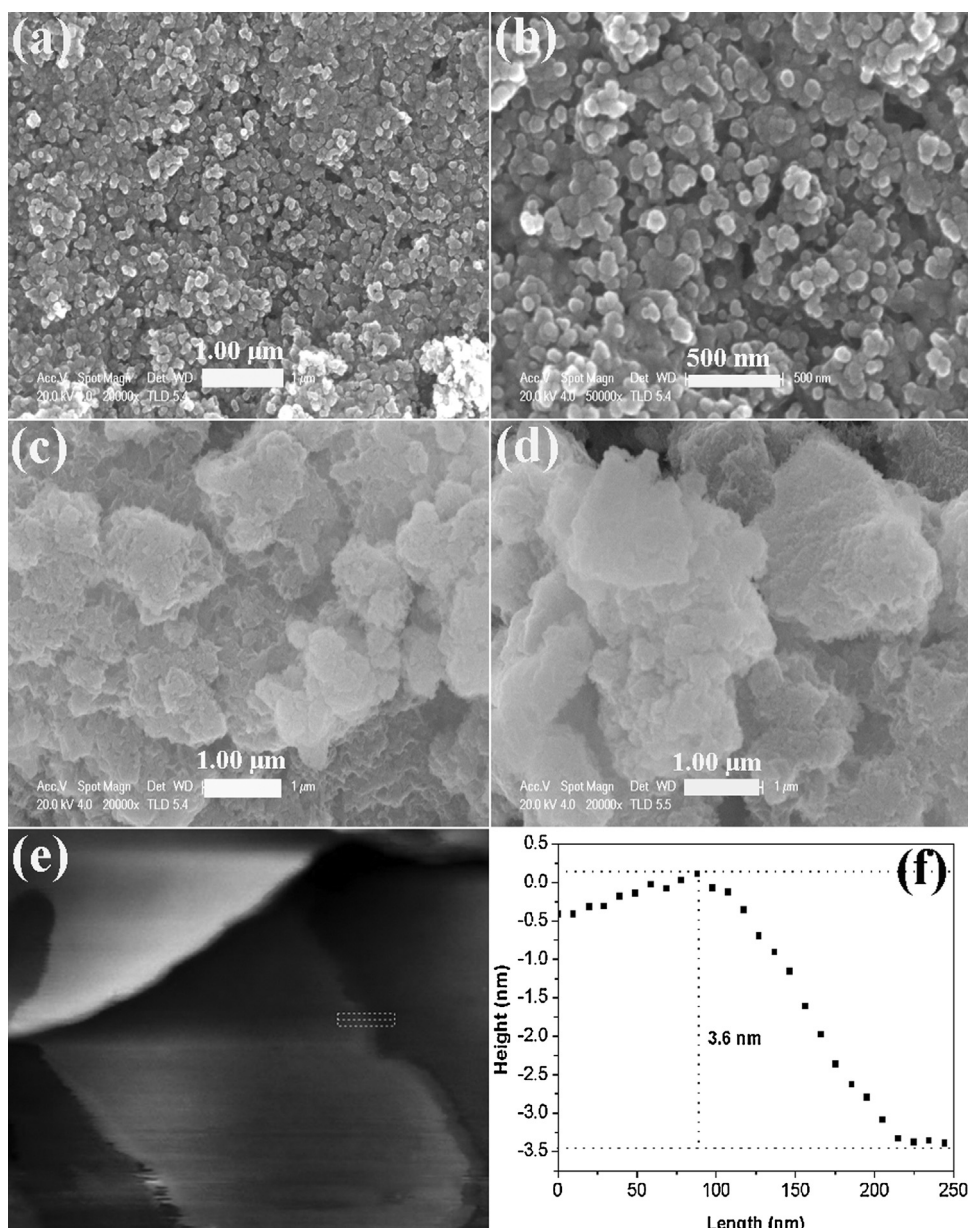


Fig. 1. SEM images of (a–b) P25, (c) TNSs, (d) 5.0%–Mn–TNSs; (e) AFM image of TNSs and (f) line profile showing the height of the TNSs.

treatment, which means that the TiO_2 nanoparticles have been stripped into nanosheets. The samples mainly consist of nanosheets with the length greater than one hundred nanometers and the width several tens of nanometers. The increasing scale of nanosheets implies that the small nanosheets stripped off from the granular crystals grow gradually, due to the oxidation of the OH species at the edge of raw nanosheets [34,35]. The HRTEM images of P25, TNSs, 2.5%–Mn–TNSs, and 5.0%–Mn–TNSs were presented in Fig. 2b,d,f,h. Comparing TNSs, 2.5%–Mn–TNSs, and 5.0%–Mn–TNSs with P25, nanosheets do not have well-developed lattice fringes or other typical crystal characteristics, showing relatively low crystallinity. From the Fig. 2d,f,h, it can be seen that Mn–TNSs have the similar sheet-like structure with the pure TNSs. In addition, it can be found that the surface of 2.5%–Mn–TNSs (Fig. 2f) is much rougher than that of TNSs. When the ratio of Mn/Ti is 5.0 at.%, small particles (about 1–2 nm) appeared on the surface of TNSs, which is the direct evidence for the loaded manganese oxides (Mn_xO_y). The EDS (the insets) in Fig. 2f and h exactly support the point, and the

distinct peaks ascribes to Ti, O, and Mn, confirming the corresponding elements in the composites.

N_2 adsorption–desorption isotherms and pore size distribution of P25, TNSs, 2.5%–Mn–TNSs and 5.0%–Mn–TNSs are measured to analyse the porous properties of the as-synthesized samples. As shown in Fig. 3, the N_2 adsorption–desorption isotherms of TNSs belong to a typical Type IV sorption behavior with a large Type H3 hysteresis loop, which represents the mesoporous structure according to the classification of IUPAC, and the mesopores mainly origin from the interspaces of the aggregated nanosheets [36]. The hysteresis loops are also observed in Mn–TNSs, and the Mn–TNSs samples show a lower absorption than pure TNSs at high relative pressure range ($0.60 < P/P_0 < 0.99$), indicating the decrease of the mesopores formed in Mn–TNSs (Fig. S1). Meanwhile, Mn–TNSs exhibit an average pore size with a narrow distribution, which is a little smaller than that of TNSs, that is probably because of the small Mn_xO_y nanoparticles dispersed into the pores of TNSs. The results were also confirmed by the decreased tendency of S_{BET}

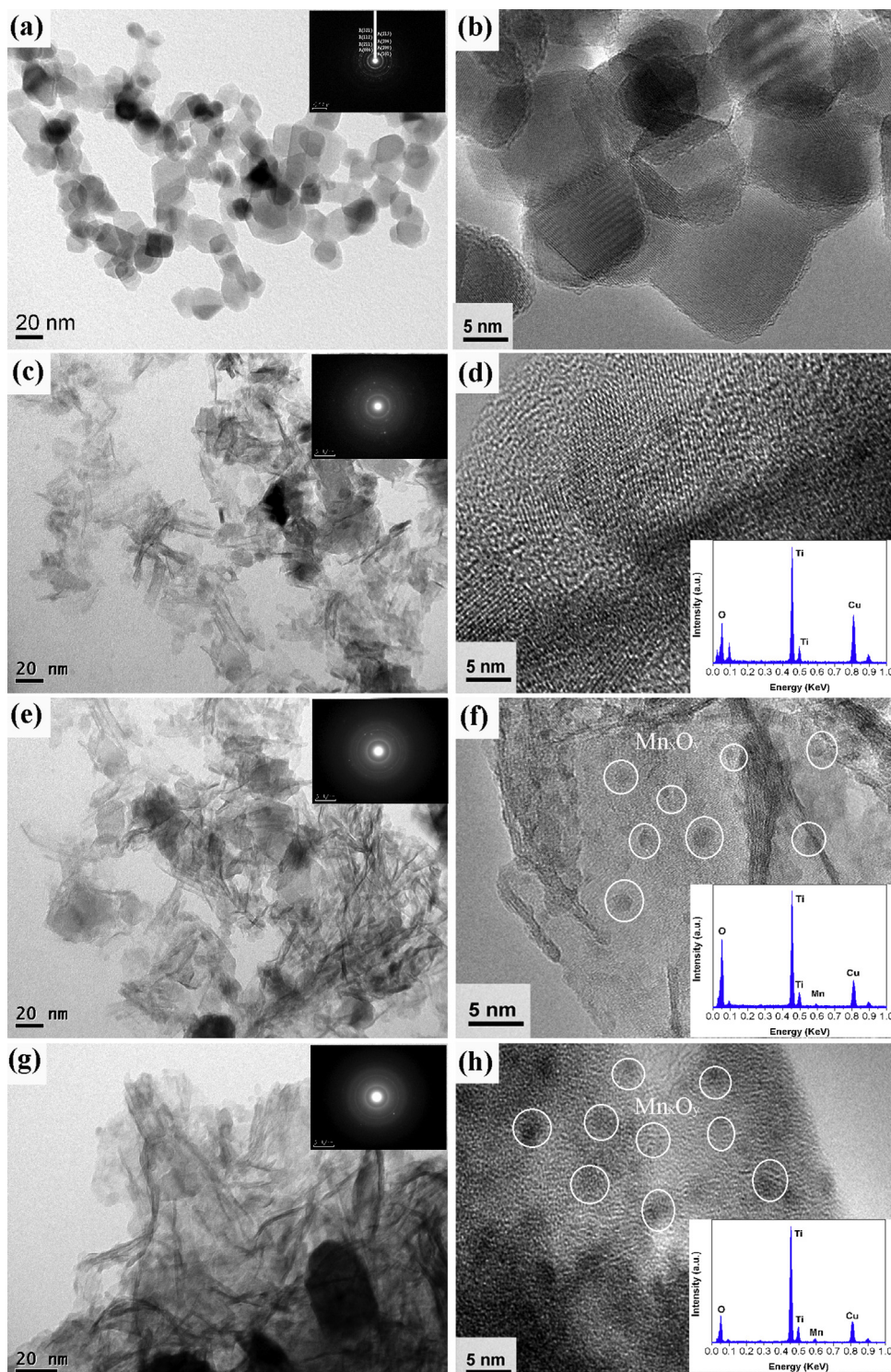


Fig. 2. TEM images, partial SAED patterns, HRTEM images, and EDS spectra of the P25, TNSs and Mn_xO_y loaded TNSs for (a–b) P25, (c–d) TNSs, (e–f) 2.5%–Mn–TNSs, and (g–h) 5.0%–Mn–TNSs.

from $342.25 \text{ m}^2/\text{g}$ of TNSs to $195.54 \text{ m}^2/\text{g}$ of 5.0%–Mn–TNSs. These results suggest that the ion-exchange in hydrothermal process make the Mn_xO_y nanoparticles enter into the interspaces of the aggregated nanosheets and block the mesopores among them, and thus decrease in S_{BET} and pore volume of TNSs (Table 1).

The crystallization of P25, TNSs, and Mn–TNSs were further identified by using wide angle XRD patterns. As shown in Fig. 4, P25 shows a miscrystal of anatase and rutile, which are in agreement with JCPDS No. 89–4921 and JCPDS No. 89–0552, respectively. After

alkaline hydrothermal treatment, the intensity of all original peaks weakens markedly, indicating as-synthesized TNSs are not well crystallized. Chang et al. have reported that the sodium titanates are probably first formed from high-crystalline titania powder through hydrothermal treatment, and then the sodium titanate products transform into TNSs of poor crystallinity after washing with HCl solution [37,38]. Moreover, as can be seen from inset in Fig. 4, with the content of Mn_xO_y increasing, the intensity of peaks A (1 0 1), R (1 0 1), A (2 0 0) and A (1 0 5) patterns increase slightly, illustrating

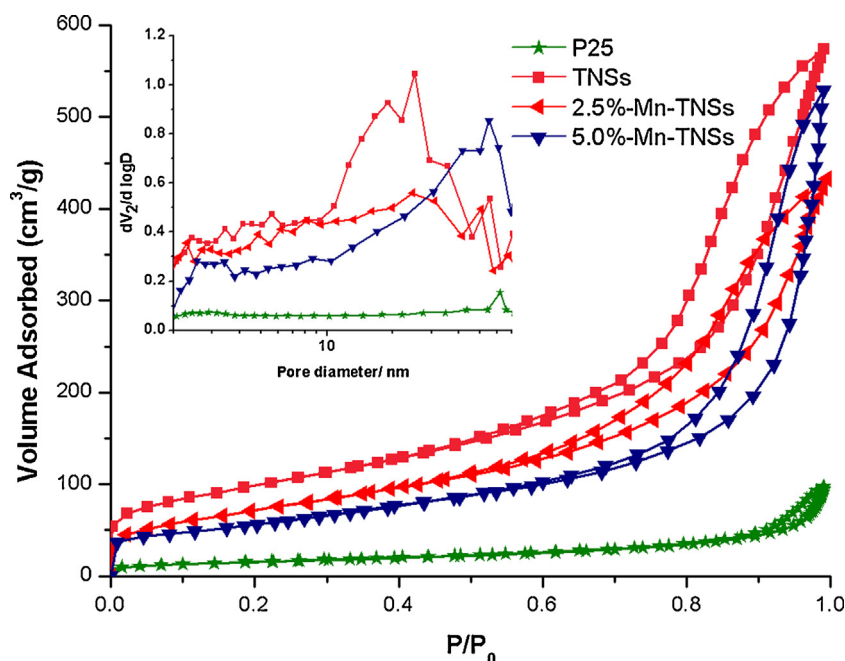


Fig. 3. The N_2 adsorption/desorption isotherms and the corresponding pore size distribution curves.

that the crystallization of samples is getting higher gradually with increasing the amount of Mn_xO_y . This phenomenon implies that loaded Mn_xO_y may inhibit slightly the transformation from P25 (3D) to TNSs (2D). However, the XRD spectra do not show the trace of Mn_xO_y . Actually, for Mn_xO_y being not observed, there are two cases: one is that Mn_xO_y does not exist in the product; the second is that amorphous Mn_xO_y has been formed. To this end, we have made further investigation; the results are shown in Fig. S2. From the analysis results in Fig. S2, it can be concluded that introduced manganese mainly exist on the surface of TNSs in the form of amorphous oxides (Mn_xO_y).

Fig. 5 presents Raman spectra of P25 and undoped TNSs. The patterns display clearly Raman peaks in the range of 100–800 cm^{-1} . As shown in Fig. 5, the peaks of 147 cm^{-1} (E_g), 197 cm^{-1} (E_g), 399 cm^{-1} (E_g) and 643 cm^{-1} (E_g) are the characteristics of anatase phase [39,40]. After alkaline hydrothermal treatment, the original peaks all weakened significantly (in the spectrum of TNSs). In addition, two new peaks at around 279 cm^{-1} (B_{1g}) and 456 cm^{-1} (E_g) in the spectrum of TNSs appeared, which were ascribed to hydrogen titanate [41]. As is well known that the sodium titanates maybe be initially formed from raw titania powder through hydrothermal treatment, and then the sodium titanate products convert to hydrogen titanate after pickling with HCl solution [21,37]. In addition,

plenty of hydroxyls groups were produced on the surface of TNSs through an ion exchange process, which can enhance the adsorption of pollutants onto adsorbents. The inset (in Fig. 5) shows Raman spectra of Mn_xO_y -loaded TNSs. From the figure it is obvious that, with the amount of Mn_xO_y increasing from 0 % to 5.0 %, the peak intensity (147 cm^{-1}) increases gradually and that the FWHM value (147 cm^{-1}) decreases slightly, which further indicate that loaded Mn_xO_y may somewhat inhibit the transformation from 3D to 2D. The results are in good agreement with that of XRD. From the main peaks 147 cm^{-1} (anatase phase), it can be seen that the vibrational frequency has slight shift with the amount of Mn_xO_y increasing. Those modes represent the Ti–O lattice vibrations. The results indicate that loaded Mn_xO_y have a remarkable impact on the Ti–O lattice of TNSs.

The surface composites and chemical states of as-prepared samples were then studied by XPS. As shown in Fig. 6a, the XPS survey spectra indicated that the samples were composed mostly of Ti, O, Mn and C elements. C element in the samples may come from the background. In Fig. 6b, the broad and asymmetric O 1s core level spectra of TNSs could be fitted by two nearly Gaussian peaks at binding energies of around 530.02 eV and 531.58 eV, respectively. The strong peak at around 530.02 eV attributes to Ti–O, and the peak at 531.58 eV may be associated with hydroxyl

Table 1
Structure parameter of P25, undoped TNSs and Mn–TNSs composites.

Samples notation	Mn/Ti molar ratio	S_{BET} (m^2/g)	APS ^a (nm)	PV ^b (cm^3/g)	BE ^c (eV)	FWHM ^d (cm^{-1})
P25	0.0%	52.41	7.31	0.151	3.22	8.21
TNSs	0.0%	342.25	10.08	0.891	3.21	13.21
0.5%–Mn–TNSs	0.5%	333.87	9.88	0.884	3.19	13.18
1.0%–Mn–TNSs	1.0%	318.23	10.07	0.865	3.13	13.11
1.5%–Mn–TNSs	1.5%	316.53	10.42	0.860	3.09	13.01
2.0%–Mn–TNSs	2.0%	271.23	9.13	0.839	3.06	12.91
2.5%–Mn–TNSs	2.5%	247.96	9.60	0.822	3.03	12.86
3.0%–Mn–TNSs	3.0%	240.10	12.33	0.813	2.99	12.81
3.5%–Mn–TNSs	3.5%	239.61	13.13	0.811	2.95	12.79
5.0%–Mn–TNSs	5.0%	195.54	15.96	0.806	2.92	12.78

^a The average pore size.

^b The BJH total pore volume.

^c The band-gap energy.

^d The FWHM of Raman peak.

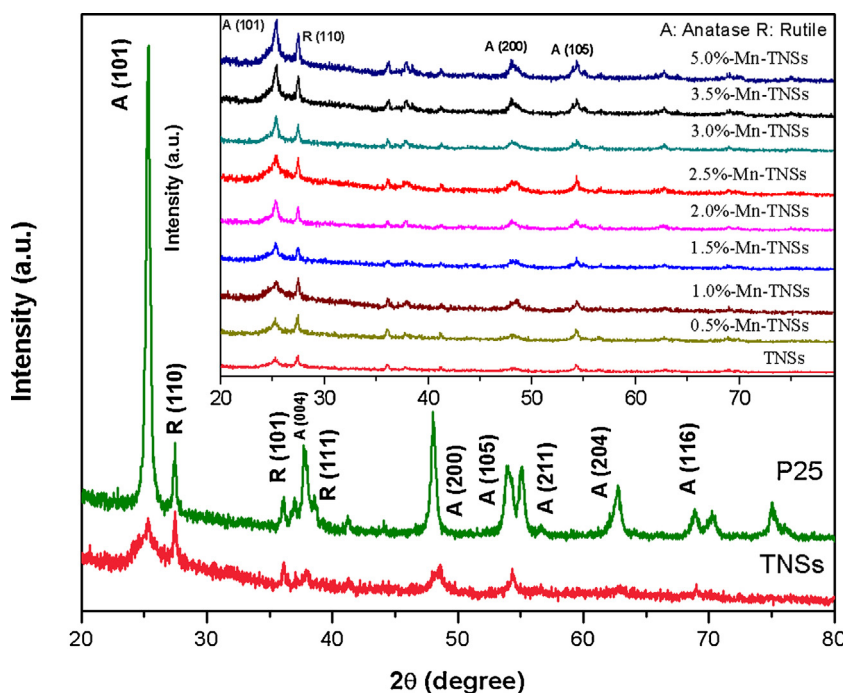


Fig. 4. XRD patterns of P25 and TNSs and the spectra (inset) of x -Mn-TNSs ($x = 0.0\%$, 0.5% , 1.0% , 1.5% , 2.0% , 2.5% , 3.0% , 3.5% , and 5.0%).

oxygen [42,43]. After loading Mn_xO_y nanoparticles, O 1s core level spectra of 5.0%-Mn-TNSs exhibits two new peaks at 528.90 eV (Mn–O) and 532.01 eV (Ti–O–Mn), suggesting the loaded Mn_xO_y mainly exist on the surface of TNSs by the connection of Ti–O–Mn bonds at the interface [43,44]. Fig. 6c shows the XPS spectra of the Ti 2p region. The Ti 2p_{3/2} and Ti 2p_{1/2} peaks are located at ~464 and ~458 eV, respectively. The dominant peak of Ti 2p of 2.5%-Mn-TNSs (or 5.0%-Mn-TNSs) were shifted towards higher BE by 0.5 eV (or 0.7 eV) with increasing loaded content of Mn_xO_y , which can be ascribed to the formation of Ti–O–Mn bonds. Fig. 7

shows the Ti 2p region may be decomposed into two contributions of Ti^{3+} (457.55 eV and 463.30 eV) and Ti^{4+} (458.30 eV and 464.05 eV) [45–47]. The concentration of Ti^{3+} and Ti^{4+} were estimated using the area of their corresponding peaks. It can be found that the concentration of Ti^{3+} increases gradually with the amount of Mn_xO_y increasing (Table 2). And in general, Ti^{3+} is considered to be a beneficial state for the photocatalytic performance. It is speculated that the reduction of Ti^{4+} takes place in the de-lamination and growth process of Mn-TNSs. During the process of mixing, the introduced manganese will be adsorbed on the surface of raw TiO_2 , and may

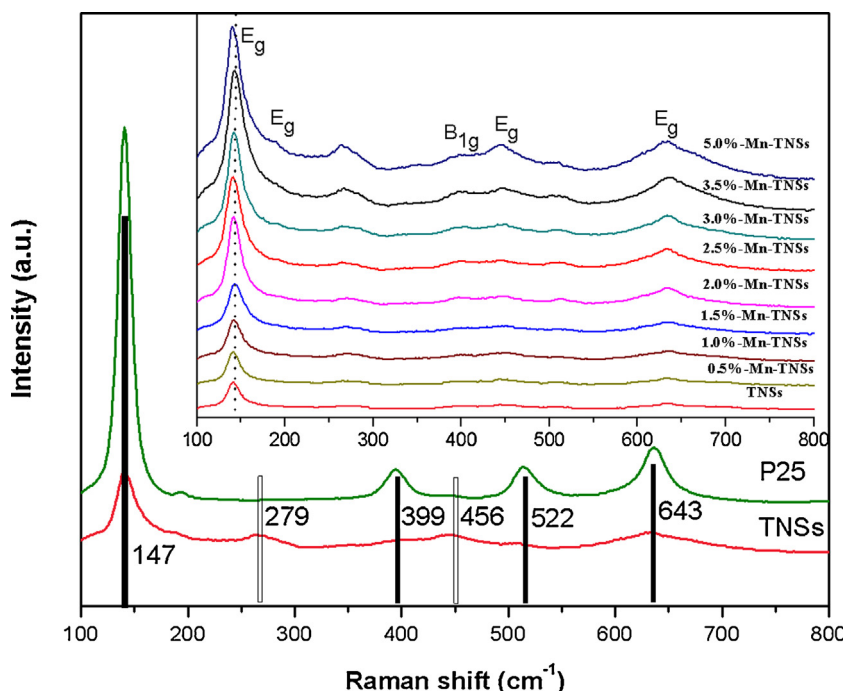


Fig. 5. Raman spectra of the P25 and TNSs and the spectra (inset) of x -Mn-TNSs ($x = 0.0\%$, 0.5% , 1.0% , 1.5% , 2.0% , 2.5% , 3.0% , 3.5% , and 5.0%).

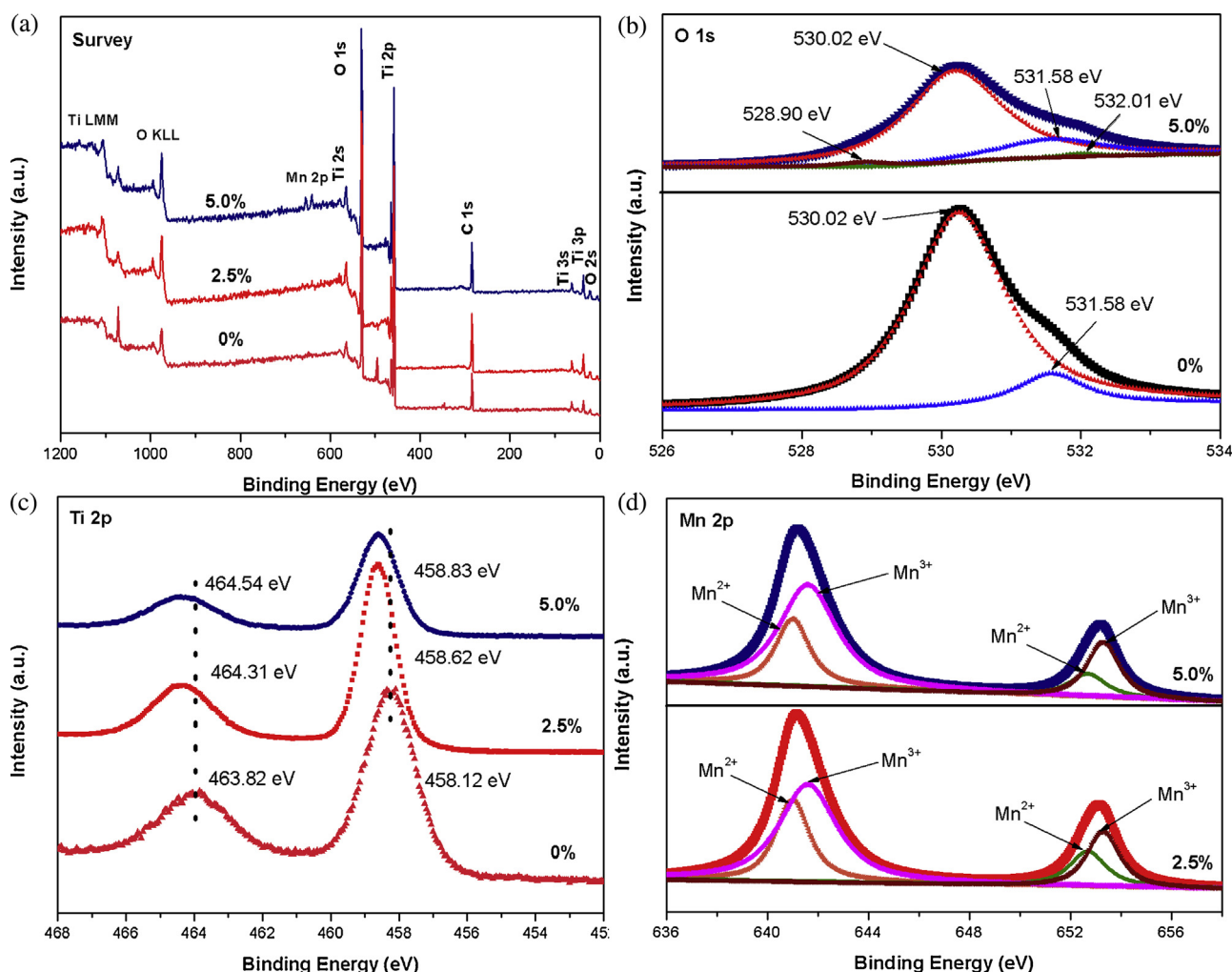


Fig. 6. XPS spectra (a) survey spectrum; (b) O 1s region of TNSs and 5.0%-Mn-TNSs; (c) Ti 2p region of TNSs, 2.5%-Mn-TNSs, and 5.0%-Mn-TNSs; (d) Mn 2p region of 2.5%-Mn-TNSs and 5.0%-Mn-TNSs.

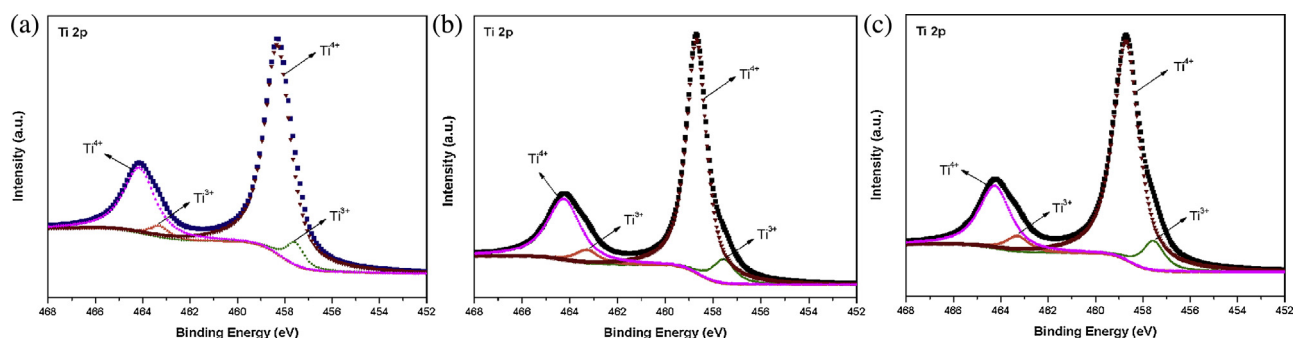


Fig. 7. The Ti 2p XPS spectra of samples (a) TNSs, (b) 2.5%-Mn-TNSs, (c) 5.0%-Mn-TNSs.

Table 2
The Ti and Mn concentration in TNSs, 2.5%-Mn-TNSs, 5.0%-Mn-TNSs.

	Samples		
	TNSs	2.5%-Mn-TNSs	5.0%-Mn-TNSs
Ti ³⁺ concentration (%)	7.87	10.4	11.7
Ti ⁴⁺ concentration (%)	92.13	89.6	88.3
Mn ²⁺ concentration (%)	–	35.2	28.1
Mn ³⁺ concentration (%)	–	64.8	71.9

influence the de-lamination of P25 and the growth of nanosheets. This may be the reason for the reduction of Ti⁴⁺ in the Mn-TNSs. Fig. 6d shows the XPS spectra of the Mn 2p region. The peaks at around 641 and 654.5 eV are ascribed to Mn 2p_{3/2} and Mn 2p_{1/2}, respectively [48,49], indicating the presence of both Mn²⁺ and Mn³⁺ ions. Mn 2p_{3/2} peak appears at 640.55 eV in 2.5%-Mn-TNSs sample, which indicates that the divalent state of Mn ions is dominant. But for 5.0%-Mn-TNSs sample, the position of Mn 2p_{3/2} peak shifted to 640.61 eV, indicating the presence of a trivalent state of Mn ions. The broadening and shifting to the higher binding energy of Mn 2p_{3/2} could be inferred from the charge transfer between Mn²⁺ and

Mn³⁺ ions. Using the area of the peak the content of Mn²⁺ and Mn³⁺ has been estimated and it can be found that the introduced manganese gives rise to the increase of Mn³⁺. The values of Mn²⁺/Mn³⁺ decrease from 54% (2.5%–Mn–TNSs) to 38% (5.0%–Mn–TNSs).

3.2. The influence of loaded Mn_xO_y nanoparticles on the structure of nanosheets

Combined with the analysis results of SEM, TEM, HRTEM, BET, XRD, Raman as well as XPS, it can be concluded that introduced manganese ions mainly exist on the surface of TNSs in the form of Mn_xO_y nanoparticles after hydrothermal treatment and proton exchange. Scheme 1(A) describes schematically the proposed formation process from original titania (3D) to Mn–TNSs (2D). Firstly, the Mn_xO_y-loaded sodium titanates were possibly formed from original P25 powder through hydrothermal treatment at 130 °C for 3 h, and then sodium titanate convert to hydrogen titanate after washing with 0.1 mol/L of HCl solution. However, with the increase in the amount of loaded Mn_xO_y, its influence on the structure of TNSs has become prominent. The mechanism behind the influence of Mn_xO_y nanoparticles on the structure of TNSs during hydrothermal process can be explained as follows. Fernando Alvarez–Ramirez et al. have mentioned the transformation process from TiO₂ powder to sheet-like TNSs [50]. Schematic representations of the different stages in the mechanism of the TiO₂ to TNSs were shown in Scheme 1(B). Under alkaline hydrothermal conditions, firstly the internal oxygen atomic layers of TiO₂ shift, and then the oxygen atoms are twisted or rotated creating an angle between them (stages of I–II). The effect of shifting–twisting process is to leave the involved oxygen atoms too close to titanium atoms to form new Ti–O bonds. As a consequence, the original three tri-coordinated oxygen atoms of TiO₂ become tetra-coordinated (T_h) oxygen (stages of III–IV). The formation of the T_h oxygen atoms induces a distortion in different layers. At this stage, there is a formation of lepidocrocite-type layers, which further joined to form a lepidocrocite array (stage of V). During the formation of the lepidocrocite bonded layers, the middle layers dislocated with respect to the external layers. If the dislocation is too large then the bonds would break forming the lepidocrocite-type layers. The common region is composed of edge-sharing TiO₆ octahedrons. At last, the sheet-like TNSs are formed by layers of an infinite sequence of the edge-sharing TiO₆ octahedrons. However, with the introduction of Mn ions, Ti–O–Mn bonds are generated, and the twisting and rotation of oxygen atoms may be inhibited up to certain extent, and the portion of tri-coordinated oxygen atoms keep original structure. Therefore, it can be interpreted that the loaded Mn_xO_y has slight influence on the structure of TNSs and the content of TiO₂ increase gradually with the amount of Mn_xO_y increasing from 0.5 at.% to 5.0 at.%.

3.3. Optical properties of the pure TNSs and Mn_xO_y-loaded TNSs photocatalysts

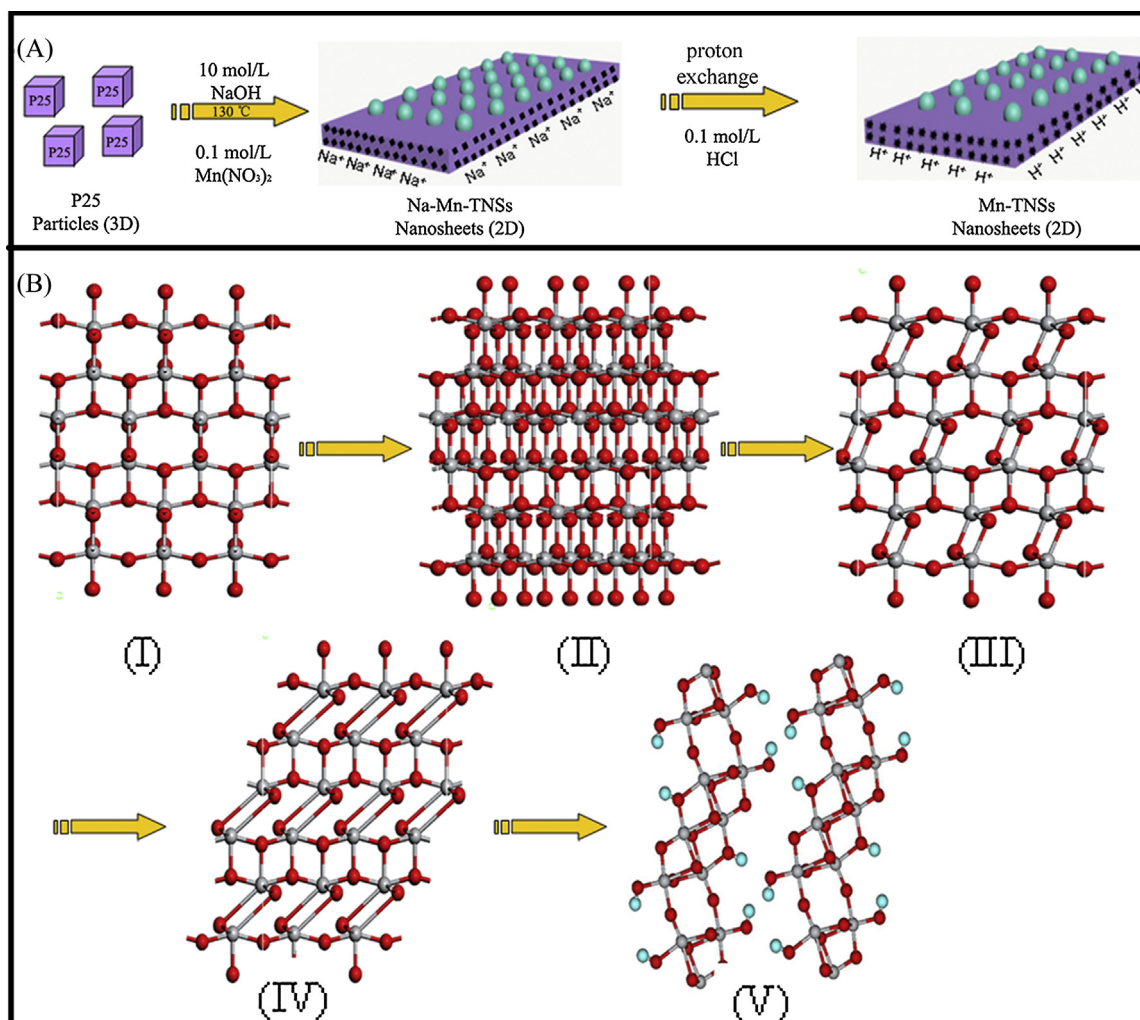
Fig. 8 shows UV–vis diffuse reflectance spectra (DRS) of as-prepared TNSs and Mn_xO_y-loaded TNSs. It can be observed that the optical absorption enhanced gradually in the visible region with the increase of the amount of Mn_xO_y nanoparticles, which can be attributed to the absorption of Mn_xO_y nanoparticles on the surface of the samples. The color variation of the photocatalysts intuitively reflects the variation of their optical absorption properties: the as-prepared samples turn from white to grey, and then into brown with increasing the amount of Mn_xO_y (Fig. 8b). Moreover, the absorption edges shift toward longer wavelengths for the Mn_xO_y-loaded samples due to the presence of Mn_xO_y particles, suggesting that the photocatalytic activity in the

visible region could be enhanced. The absorption data are fitted to equation for indirect band–gap transitions: $(\alpha h\nu)^{1/2} = A(h\nu - E_g)$, where α is the absorption coefficient, $h\nu$ is photon energy, E_g is the band gap, and A is constant. The band-gap energy of samples can be estimated from the x-intercept of the tangents, and the E_g values are listed in Table 1. It clearly shows that the corresponding band-gap energies of the samples decrease with the loaded amount of Mn_xO_y nanoparticles increasing. The decrease in the band-gap energy of Mn_xO_y-loaded samples compared to the bare one also could be attributed to the existence of Mn_xO_y nanoparticles.

Fig. 9a shows the fluorescence spectra of TNSs and Mn_xO_y-loaded TNSs using excitation of 300 nm. It can be seen that the FL intensities of x–Mn–TNSs ($x = 0.0\%$, 0.5% , 1.0% , 1.5% , 2.0% , 2.5% , 3.0% , and 3.5%) are lower than that of undoped TNSs. As is well known that the FL emission spectra have been widely applied to study the efficiency of photo-generated charges trapping, transfer, and separation in semiconductor. Lower FL emission intensity indicates a lower recombination rate of photo-generated electron–hole pairs [51]. Therefore, it can be deduced that the recombination efficiency of x–Mn–TNSs ($x = 0.0\%$, 0.5% , 1.0% , 1.5% , 2.0% , 2.5% , 3.0% , and 3.5%) were relatively lower than that of 5.0%–Mn–TNSs under visible-light irradiation. Moreover, with increasing the loaded amount of Mn_xO_y, the FL emission intensity initially decreases, and then increases after attaining a minimum value at 2.5%–Mn–TNSs (Fig. 9b). It can be assumed that Mn_xO_y nanoparticles with appropriate content can act as electron traps, thus would enhance the separation efficiency of photo-generated electron–hole pairs; whereas when the Mn_xO_y loading concentration is too high, too much Mn_xO_y nanoparticles would turn into recombination centers of the photo-generated electron–hole pairs during the photocatalytic reactions.

3.4. Photocatalytic activity evaluation

Fig. S3 shows a comparison of the adsorption performances of P25, TNSs, and Mn_xO_y loaded TNSs towards RhB solution with a concentration at 20 mg/L, and the adsorption process was performed in the absence of light (dark experiment). As shown in Fig. S3, it can be clearly found that the as-synthesized TNSs possess good adsorption ability towards RhB, and the adsorption capacity of TNSs (9.41%) is ca. 1.8-fold as high as that of the P25 (5.23%). Besides, the adsorption capacity of Mn–TNSs increases initially with the Mn/Ti atomic ratio increasing to 2.5 at.%, and then it decreases with the further increasing. The highest adsorption capacity was obtained at the loading amount of 2.5 at.%, with 20.7% RhB adsorbed after 60 min in dark experiments. It is generally accepted that the adsorption capacity of photocatalysts were not only associated with S_{BET} that allowed the catalyst to adsorb pollutants largely, but also closely related to their surface states. Many earlier reports suggested that the enhancement of adsorption resulted from the increase of surface acidity after being modified by semiconductor photocatalyst [52,53]. F. Chen et al. have pointed similar work on AgO₂ modified-TiO₂ system that possesses higher adsorption capacity than bare TiO₂, which was ascribed to the increase of acid sites on photocatalyst surface [53]. The large specific surface area provided both better adsorption of RhB and promoted the formation of more adsorption sites on the modified TNSs surface. Therefore, though the specific surface area of TNSs modified by Mn_xO_y is smaller than that of TNSs (shown in Table 1), 2.5%–Mn–TNSs still possesses highest adsorption capacity among all samples. Hence, the change of adsorption capacity of samples may be explained as follows: when the loading ratio of Mn/Ti increased from 0.0 at.% to 2.5 at.%, the increasing of adsorption sites of Mn–TNSs was dominant, and so the adsorption capacity increased.



Scheme 1. (A) The proposed formation mechanism of Mn-TNSs. (B) Schematic representation of the different stages in the mechanism of the TiO₂ to TNSs: (I) and (II) are initial configurations, where the initial atomic shifts and oxygen atom twisting are indicated; (II) This is a slightly rotated view of crystal shown in (I); (III) This figure shows the structure shifted and twisted where the formation of tetracoordinated (T_h) oxygen atoms is indicated; (IV) After formation of the T_h oxygen atoms, the crystal structure is distorted as shown here; (V) TNSs are formed here.

With further increase of loading ratio, the S_{BET} of samples decreased drastically, resulting in the decrease of adsorption capacity.

The photocatalytic activities of all samples are evaluated by the degradation of RhB solution (20 mg/L) under visible-light irradiation. The blank test without any catalysts indicates that RhB molecules were relatively stable and the photolysis process is neglectable. For comparison, unloaded TNSs are also tested by the same way. The experimental results are shown in Fig. 10. The absorbance spectra of RhB solution using 2.5%–Mn-TNSs as a representative are shown in Fig. 10a. The rapid decrease in the concentration of RhB solution and a blue shift in absorbance peak were found to co-exist, which reveal a simultaneous decomposition in the conjugated structure and demethylation during the photoreaction process. From Fig. 10b, it is obvious that when the amount of Mn_xO_y is relatively low (≤ 2.5 at.%), the visible-light photocatalytic activities increase gradually with the increase of loaded amount, and the photocatalytic activity of 2.5%–Mn-TNSs reaches maximum, demonstrating that optimal loaded ratio of Mn_xO_y is 2.5 at.%. With further increasing the loaded amount of Mn_xO_y, the photocatalytic activities of samples decrease gradually under visible-light irradiation. The photocatalytic activity of 5.0%–Mn-TNSs is lower than pure TNSs. As shown in Fig. 10c–d, the experimental data

is found to be in accordance with the first-order kinetic equation ($\ln(C_t/C_0) = -K_{\text{app}}t$), where K_{app} is the apparent rate constant, C_0 , the initial concentration of solution, t , the reaction time, and C_t is the concentration of solution at the reaction time of t . It is found that the reaction rate K_{app} of 2.5%–Mn-TNSs is 6.87-fold of that of TNSs under visible-light irradiation. Therefore, it can be noted that appropriate loaded amount of Mn_xO_y (≤ 2.5 at.%) can enhance the photocatalytic activity of samples effectively; when the loaded amount is higher than the optimal value of 2.5 at.%, loaded Mn_xO_y nanoparticles becomes detrimental. The results of photocatalytic activity are in coincidence with that of the photo-generated electron–hole pairs recombination from the FL spectra. Moreover, the photocatalytic activity of samples under UV–vis light irradiation was displayed in Fig. S4. Fig. S4a–c indicates that the photocatalytic activity of samples under UV–vis light irradiation and visible-light photocatalytic activity show the similar trend.

The cyclic performance of the Mn_xO_y-loaded TNSs was further investigated to evaluate their stability. Since 2.5%–Mn-TNSs show the highest photocatalytic activity for photodegradation of RhB solution, it was chosen to investigate the cyclic performance. As shown in Fig. S4d, after five cycles of the photodegradation of RhB, the 2.5%–Mn-TNSs photocatalyst does not exhibit any significant loss of photocatalytic activity. The result of the cyclic experiment

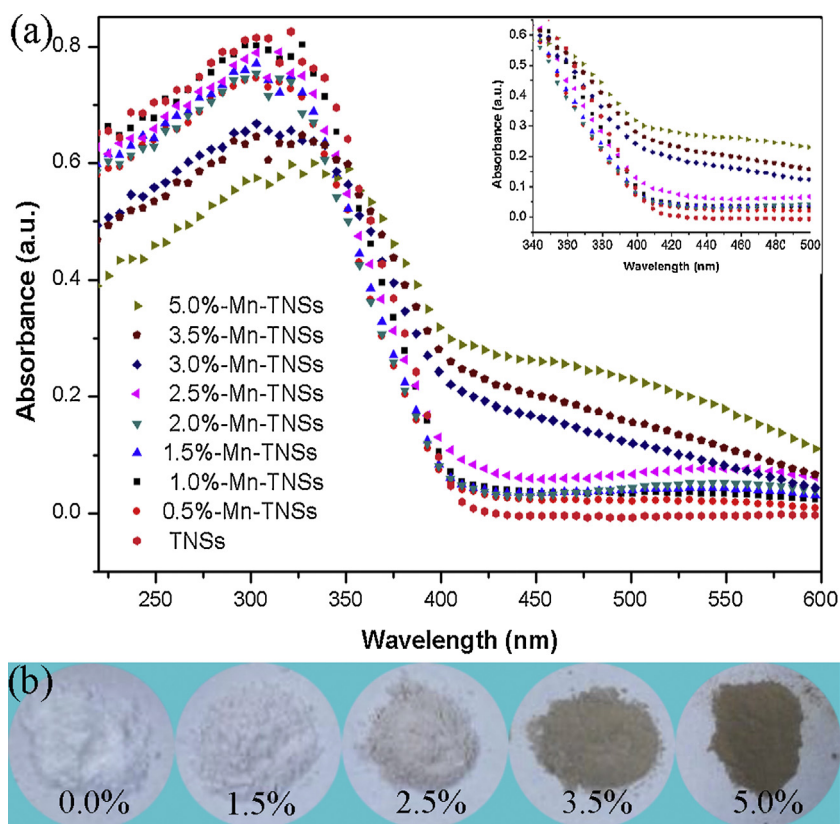


Fig. 8. (a) UV-vis diffuse reflectance spectra and corresponding colors of as-prepared bare TNSs, and Mn_xO_y-loaded TNSs with a varying Mn/Ti molar ratio.

indicates that the Mn_xO_y-loaded TNSs are relatively stable during the photocatalytic oxidation of the pollutant molecules.

The photocatalytic reduction of Cr(VI) in K₂Cr₂O₇ aqueous solution was employed as toxic heavy metals' pollutions to evaluate the photocatalytic activity of as-prepared samples under visible-light irradiation. Fig. 11 demonstrates the photocatalytic reduction of Cr(VI) and the reaction constant over various as-synthesized samples at pH 1 under visible-light irradiation. After being exposed to visible-light irradiation for 70 min, there was no observable decrease in Cr(VI) amount for TNSs, denoting that the raw TNSs has barely any visible-light photocatalytic activity for Cr(VI). Conversely, it can be found that α -Mn-TNSs ($\alpha = 0.5\%$, 1.0% , 1.5% , 2.0% ,

2.5% , 3.0% , and 3.5%) have higher photocatalytic efficiency than that of pure TNSs. It can be deduced that the samples loaded Mn_xO_y were beneficial for the photocatalytic reduction of Cr(VI). Moreover, with the loaded amount of Mn_xO_y increasing, the visible-light photocatalytic activity of TNSs were significantly improved, and reaches to a maximum with the Mn_xO_y concentration at 2.5 at.%. However, the photocatalytic activity decreases rapidly when the concentration of Mn_xO_y is higher than 2.5 at.%. In order to further research and study, a kinetic simulation is made. The results show that the reactions obey the first-order relationship ($\ln(C/C_0) = -K_{app}t$), similar to the photodegradation of RhB in aqueous solution. By calculating the slope, the reaction rate constant (K_{app}) values are

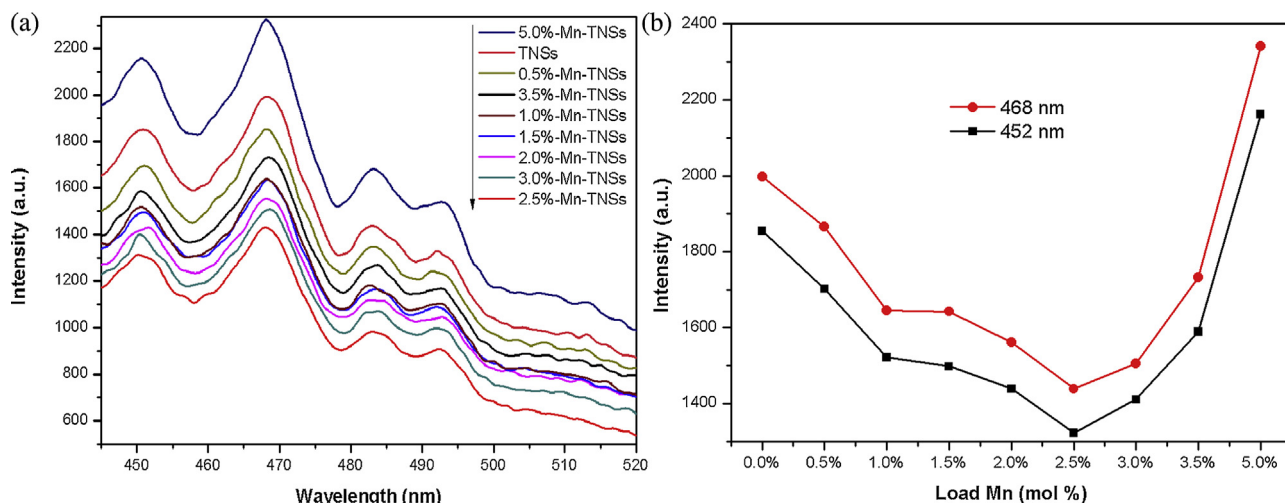


Fig. 9. (a) Fluorescence spectra of TNSs and Mn_xO_y-loaded TNSs using excitation of 300 nm; (b) fluorescence intensity at 452 nm and 468 nm as a function of loaded amount.

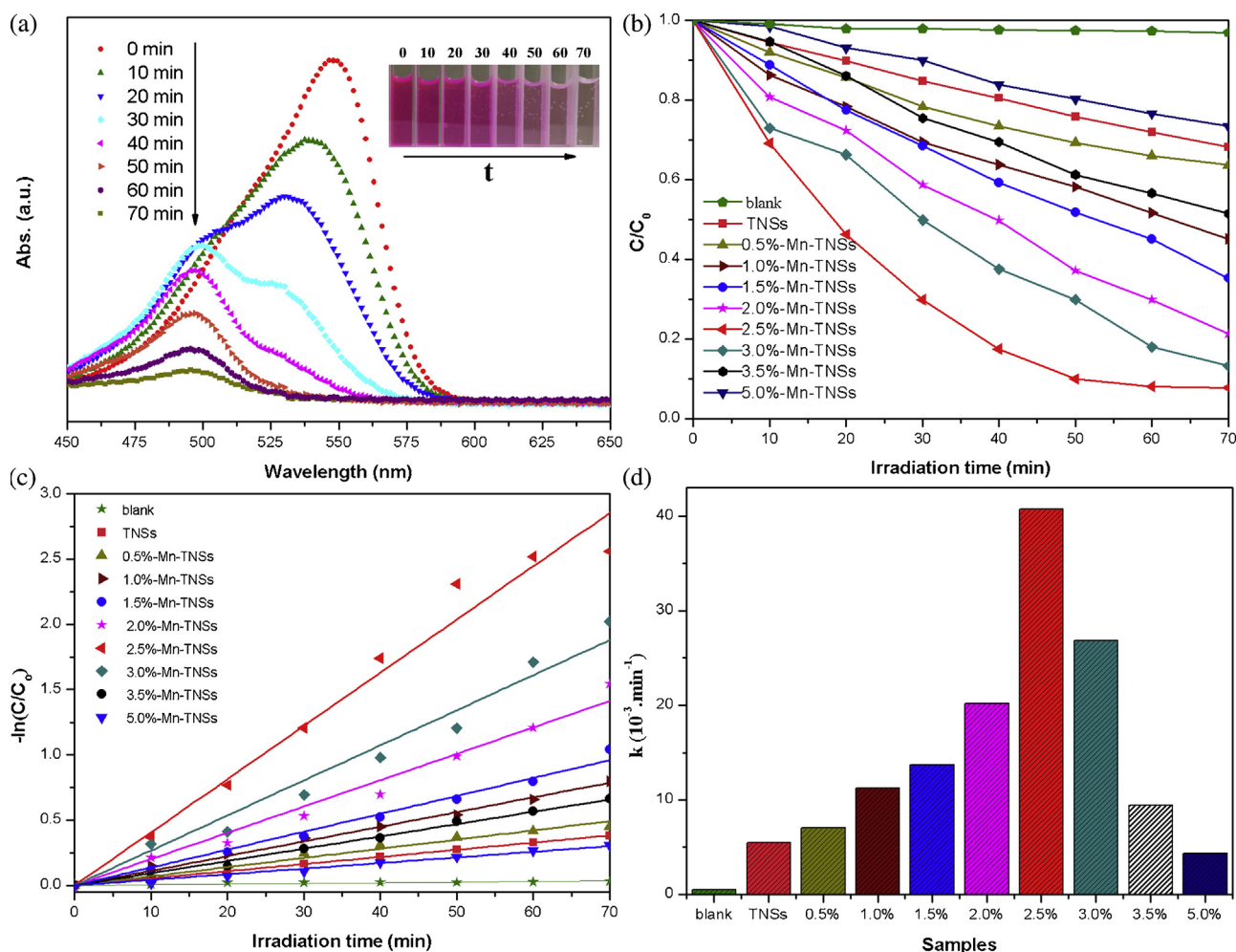


Fig. 10. Visible-light photocatalytic performance evaluation: (a) photodegradation of RhB using 2.5%-Mn-TNSs; (b) photocatalytic degradation of RhB under visible-light irradiation; (c) reaction kinetics ($\ln(C/C_0) = -K_{app}t$) of visible-light photoreaction; (d) the reaction rate constant (K_{app}) values under visible-light irradiation.

obtained (Fig. 11b). A comparison of the K_{app} values indicates that the photocatalytic degradation rate of 2.5%-Mn-TNSs is 2.37-fold of that of TNSs. In addition, the photocatalytic activity of samples under UV-vis light irradiation was displayed in Fig. S6. From the Fig. S(6a–6b), it can be found that the photocatalytic activity of

samples under UV-vis light irradiation show the same trend with that of visible-light photocatalytic activity.

Further, in order to study the synergistic photocatalytic removal of Cr(VI) and RhB, 2.5%-Mn-TNSs were evaluated by simultaneous photocatalytic decontamination of Cr(VI) and RhB under visible-

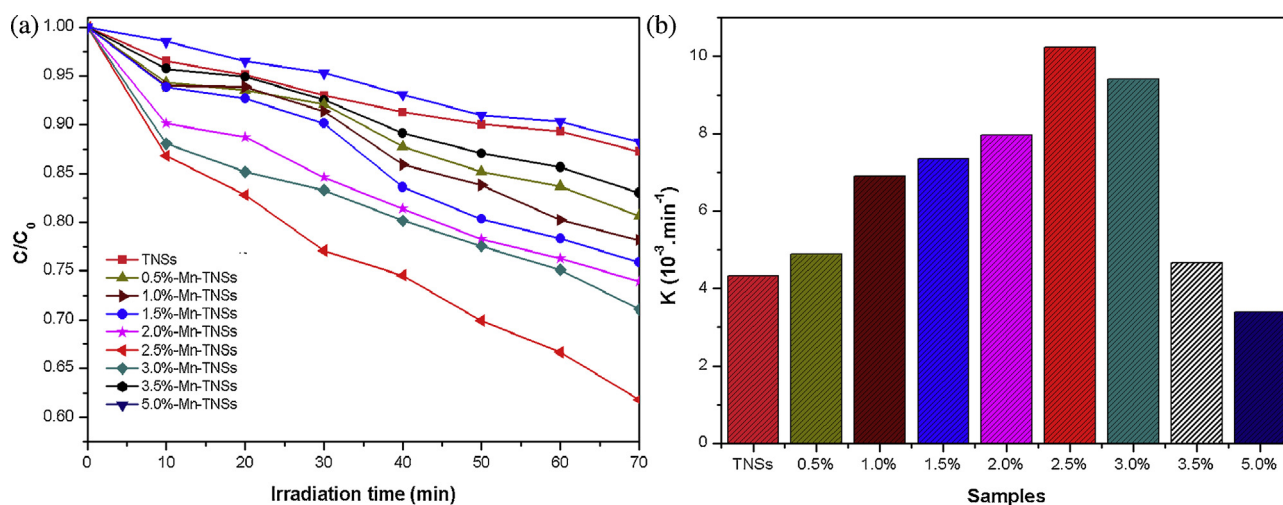


Fig. 11. (a) Photocatalytic reduction of Cr(VI) by different samples under visible-light irradiation; (b) the reaction rate constant (K_{app}) over different samples. Initial concentration of Cr(VI) was 50 mg L^{-1} , the dosage of photocatalyst was 1 g/L , and pH was 1.

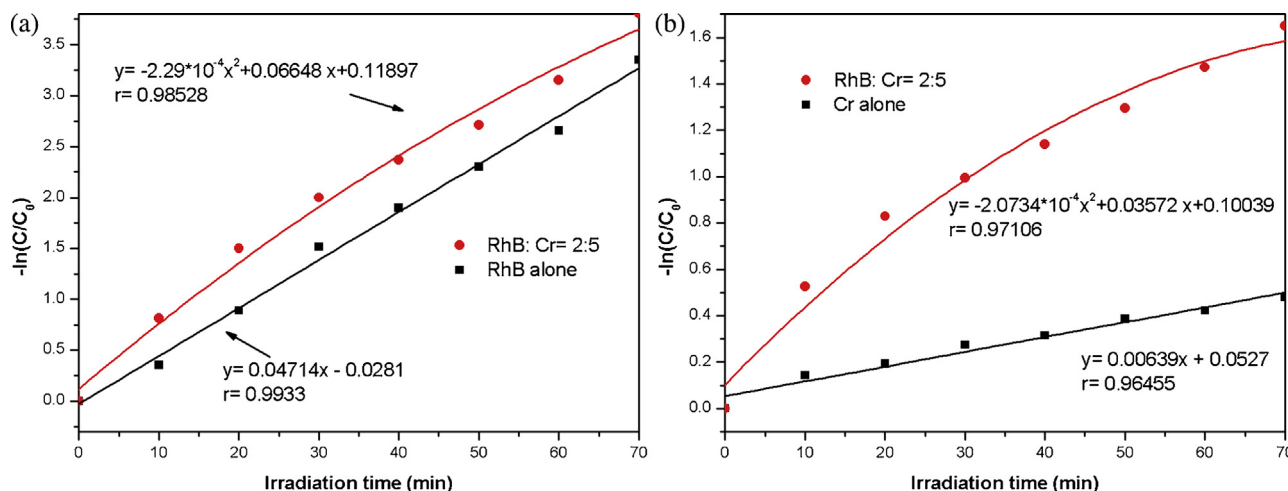


Fig. 12. (a) Kinetics of RhB degradation in the absence or present of Cr(VI); (b) Kinetics of Cr(VI) degradation in the absence or present of RhB. Initial concentration of RhB and Cr(VI) was 20 mg L⁻¹ and 50 mg L⁻¹, the dosage of photocatalyst was 1 g/L, and pH was 1.

light irradiation. The degradation profiles of RhB, with an initial concentration of 20 mg/L, in the absence and presence of Cr(VI) at 50 mg/L is shown in Fig. 12a. From the figure, it can be found that the presence of Cr(VI) leads to an increase in the rate of RhB degradation. The addition of Cr(VI) results in a kinetic constant, during the first 40 min over 1.5-fold as high as that of isolated RhB. Moreover, it can be found that the extent of RhB degradation also increased as a result of Cr(VI) addition. The improvement in the rate and extent of RhB degradation indicates that Cr(VI) is an efficient scavenger of photo-generated electrons. Conversely, when the photocatalyst was absent, there was no significant reaction between Cr(VI) and RhB under homogeneous conditions at pH 1. Theoretically, it has been shown that, in this kind of photochemical process, the number of charges involved in the oxidation and reduction semi-reactions must be equal and therefore one can anticipate that the promoting effect is mutual. The rate of RhB degradation in the presence of Cr(VI) decreased after 40 mins of irradiation, due to the presence of another electron acceptor oxygen, which can compete the electron from RhB with Cr(VI) since the concentration of Cr(VI) decreased sharply. Similarly, the presence of RhB significantly promoted the reduction rate of Cr(VI) as shown in Fig. 12b. The rate of Cr(VI) reduction was found three-fold higher in the presence of RhB than in its absence.

3.5. The mechanism for the enhanced photocatalytic activity of Mn_xO_y loaded samples

The $\cdot\text{OH}$ radicals derived from oxidation of OH⁻ ions (or H₂O molecules) by the photo-generated holes (h⁺) or the photo-generated electron-induced multistep reduction of O₂⁻ radicals are considered to be the major active species responsible for photocatalytic reaction [54,55]. Further to distinguish the influence of Mn_xO_y loading, the photocatalytic production efficiency of $\cdot\text{OH}$ radicals was detected by monitoring the time-dependent generation of 7-HC. Fig. 13a shows the plots of increase in fluorescence intensity against illumination time at 450 nm for all the bare and Mn_xO_y-loaded samples. Generally, fluorescence intensity is proportional to the amount of photo-generated hydroxyl radicals. The increase in PL intensity of P25 and TNSs are too slow and almost negligible, suggesting that hydroxyl radicals can be hardly produced with the bare sample under visible-light irradiation. However, a gradual increase in PL intensity for all the Mn_xO_y-loaded samples is observed with increasing the visible irradiation time, which indicates that the photocatalysts produced the hydroxyl radicals in

proportion to the irradiation time. It can be seen that after visible irradiation for 30 mins, all the Mn_xO_y-loaded samples show improved rate of formation comparing with the bare one. It can be concluded that the loading of Mn_xO_y can significantly promote the photo-generation of $\cdot\text{OH}$ radicals, thus enhancing the photocatalytic activity. Moreover, the rate of formation of $\cdot\text{OH}$ radicals increases first and then decreases with increasing Mn_xO_y loading amount, and the formation rate of $\cdot\text{OH}$ radicals with 2.5%-Mn-TNSs is the highest, which is 3.61-fold, and 2.13-fold of that with P25 and TNSs, respectively (Fig. 13b). The tendency is well consistent with the results of the photocatalytic evaluation.

To explain the changes in photocatalytic activity under visible-light irradiation, the excitation and transfer process of charges between Mn_xO_y and TiO₂-based nanosheets is schematically illustrated in Scheme 2. The better photocatalytic activity is mainly attributed to the formation of micro-heterostructure between TiO₂-based nanosheets and Mn_xO_y nanoparticles. The charges separation and transfer of the photocatalysts of Mn_xO_y-loaded TNSs in the process of degradation of RhB was showed in Scheme 2 (a). Firstly, under the visible-light irradiation, Mn_xO_y nanoparticles can be excited to produce photo-generated electron-hole pairs, and then followed by electrons injection from excited Mn_xO_y into the conduction band of TNSs [Eqs. (1)–(2)]. Thus, the recombination of electron-hole pairs can be effectively suppressed. In both the cases, O₂ captures the reactive electrons gathering in the conduction band of TNSs to yield $\cdot\text{OH}$ radical anion and H₂O₂ [Eqs. (3)–(6)], and $\cdot\text{OH}$ radicals can be formed by the reaction between these new intermediates [Eqs. (7)–(8)]. The generation of $\cdot\text{OH}$ radicals plays a significant role in the photocatalytic reactions, as the $\cdot\text{OH}$ radicals are key reactive oxygen species in photocatalytic oxidation of RhB molecules. Apart from this, an excess of holes are left on the irradiated Mn_xO_y nanoparticles immediately after the transfer of electrons into the conduction band of TNSs. The oxidation on Mn_xO_y nanoparticles may also be due to the direct reaction between photo-generated holes and adsorbed organics (e.g., RhB molecules). As the result, the final products of RhB oxidation, CO₂ and H₂O, are formed by a series of possible reactions.

Secondly, the surface RhB molecules can absorb the energy of visible light irradiation, and then may inject electrons into the conduction bands of TNSs. The DRS results show the TNSs can not absorb visible light. Therefore, the visible photocatalytic activity of pure TNSs is mainly due to the self-sensitive decomposition of RhB molecules. The excited RhB molecules will inject electrons into the

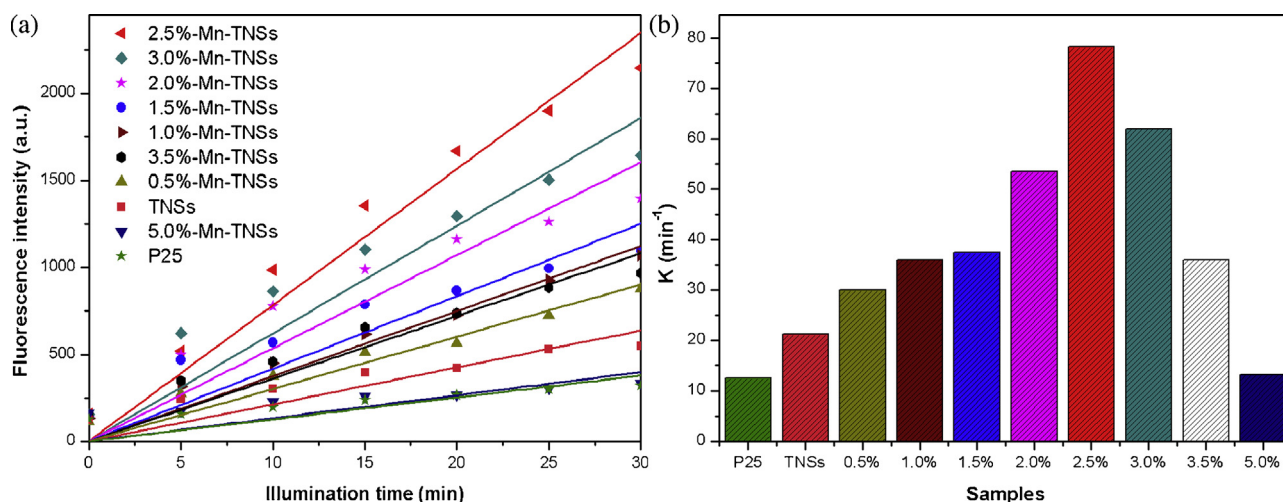
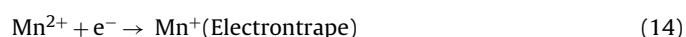
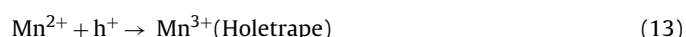
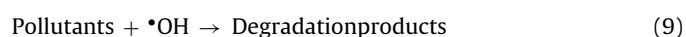
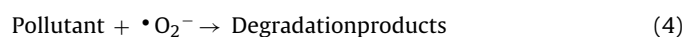
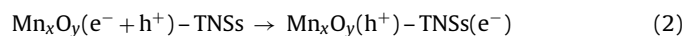
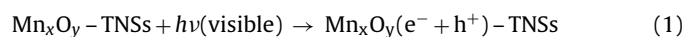
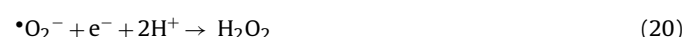
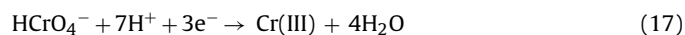


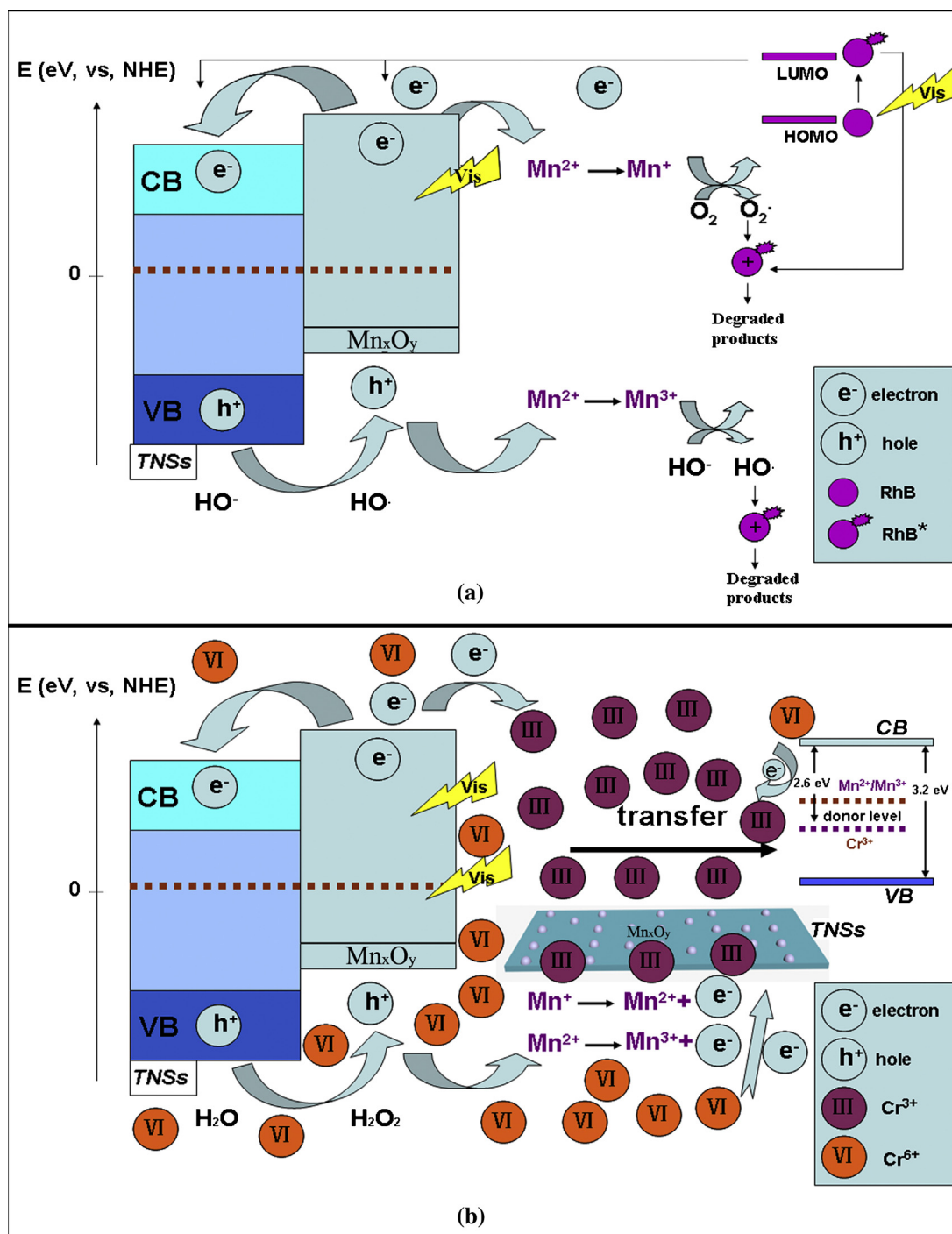
Fig. 13. (a) Formation of 7-hydroxycoumarin (monitored by fluorescence emission) in the suspensions of the bare and Mn_xO_y -loaded samples; (b) the formation rate constants of 7-hydroxycoumarin over different samples.

conduction bands of pure TNSs. When it comes to Mn_xO_y loaded TNSs, the excited RhB will inject electrons into the conduction bands of TNSs or Mn_xO_y [Eqs. (10)–(12)]. The electrons injected into the conduction bands of TNSs will participate in the photo-reaction processes described above [Eqs. (3)–(9)]. Thirdly, according to the crystal field theory, due to the half-filled d orbital (d^5), Mn^{2+} is relatively stable than Mn^{3+} and Mn^+ ions. Hence, the trapped charges can easily release from Mn^+ or Mn^{3+} and then transfer to the surface to initiate the photocatalytic reaction. Mn^+ can be oxidized to Mn^{2+} by transferring electrons to absorbed O_2 on the surface of sample [Eqs. (13)–(15)]. Meanwhile, the adsorbed O_2 is reduced to $\text{O}_2^{\cdot-}$ [Eq. (3)], which can further degrade RhB shown in Scheme 1 (a). Similarly, Mn^{3+} also are reduced to Mn^{2+} , while surface hydroxyl group translates into hydroxyl radical [OH^{\cdot}] [Eq. (16)]. Thus, photo-generated superoxide ion ($\text{O}_2^{\cdot-}$) and hydroxyl radical (OH^{\cdot}) are highly reactive when degrade the RhB solution [56]. These processes not only can accelerate the interfacial charge transfer rate, but also enhance the generation of highly reactive oxidative species such as superoxide and hydroxyl radicals.

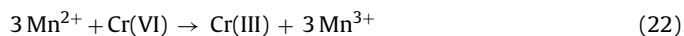
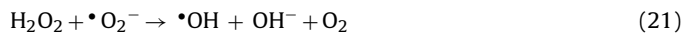


Scheme 2 (b) shows the schematic diagram for the charge separation and transfer of the Mn_xO_y -loaded TNSs in the process of degradation of Cr(VI) under visible-light irradiation. For the removal of Cr(VI) in reaction systems, firstly, when illuminated by visible light, Mn_xO_y nanoparticles were excited to produce photo-generated electron-hole pairs, followed by electrons injection from excited Mn_xO_y into the conduction band of TNSs [Eqs. (1)–(2)]. Then absorbed Cr(VI) on the sample was reduced to Cr(III) by electrons [Eq. (17)], and H_2O accepted holes in the absence of reducing agents [Eqs. (18)–(21)]. Thereby, the photocatalysis redox cycle continued. In the photocatalysis process, a portion of Cr(III) would be adsorbed onto Mn_xO_y nanoparticles by the hydroxyl groups (OH) on the surface. Nevertheless, Cr(III) was mainly adsorbed by TNSs when the adsorption process commenced. Secondly, in the reaction system, Cr removal process would be greatly different because of simultaneous performance of photocatalysis and adsorption [57,58] processes. The synergistic effects in this system could be identified in terms of coordination of Mn_xO_y and TNSs. In the system with both Mn_xO_y and TNSs, Cr(VI) on the surface of sample was reduced to Cr(III) by photo-induced electrons, and Cr(III) was immediately adsorbed by TNSs owing to their high adsorption capacity and quick kinetics. The transfer of Cr(III) from Mn_xO_y to TNSs resulted in continuous release of abundant photocatalytic sites of Mn_xO_y and exposure to Cr(VI), and thus enhanced photocatalysis. The close collaboration between Mn_xO_y and TNSs in the Cr removal process made it possible to promote photocatalytic reduction of Cr(VI) with ideal receivers of Cr(III) by TNSs adsorption. Thirdly, another aspect need to mention is the role of Cr(III) as an inhibitor. Cr(III) entered into TNSs via ion-exchange with H^+ located in the inner layers of TNSs. The entered Cr(III) could limit the recombination of electrons and holes, thus promoting photocatalytic activity of sample [50]. In addition, when Cr(III) entered into TNSs at later stage, a donor level (2.6 eV) formed in the forbidden band of TNSs, which would enhance the photocatalytic ability of sample and thus allowed the TNSs–Cr(III) to photoreduce Cr(VI) to certain extent, which is one of the important reasons for synergetic effects.





Scheme 2. Schematic diagram for the charge separation and transfer of the photocatalysts of Mn_xO_y -loaded TNSs in the process of degradation of RhB (a) and in the process of degradation of dichromate (b) under visible-light irradiation.



The characteristic enhancement of photocatalytic reduction of Cr(VI) and oxidation of RhB at 2.5%–Mn–TNSs for the mixed system is schematically illustrated. Cr(VI) as a strong oxidant can rapidly consume photocatalytically generated electrons at the conduction band of samples while RhB as an oxidisable organic matter consumes the photocatalytically generated holes at the valence band thereby giving rise to an effective suppression of the charge

recombination leading to a dramatic enhancement in photocatalytic efficiency when compared to the single systems.

6. Conclusions

A facile one-pot hydrothermal method is proposed for synthesis of TiO_2 -based nanosheets loaded with highly dispersed Mn_xO_y ($\text{Mn} = \text{Mn}^{2+}, \text{Mn}^{3+}$) nanoparticles. The as-synthesized samples are confirmed to possess high specific surface area of about $200 \sim 300 \text{ m}^2/\text{g}$, and small thickness (ca. 4 nm). The Mn_xO_y nanoparticles loaded on the nanosheets are 1–2 nm in diameter and

mainly exist in the form of divalent and trivalent, which made the absorption edges shift toward longer wavelengths and enhanced the visible-light absorption for the nanosheets. Loading of Mn_xO_y nanoparticles remarkably enhances the photocatalytic activities of the TNSs for both the aqueous RhB or Cr(VI) solution under visible-light irradiation. Moreover, the photocatalytic activity increases gradually with increasing the loaded content of Mn_xO_y nanoparticles initially, and then decreases at the Mn/Ti molar ratio of 2.5 mol.% for photocatalytic degradation of RhB and photocatalytic reduction of dichromate solution, respectively. It can be attributed to the excess Mn_xO_y may aggregate to act as the recombination site and prevent photocatalytic activity of the TNSs host by covering its surface. Therefore, the optimal content of loaded Mn_xO_y nanoparticles should be explored for achieving the highest photocatalytic activity. The results obtained from the application of 2.5%–Mn–TNSs for simultaneous photocatalytic decontamination of Cr(VI) and RhB demonstrated a strong synergistic effect that dramatically enhanced both Cr(VI) reduction and RhB oxidation removal efficiencies. An alternative possible mechanism for the enhancement of the visible-light photocatalytic activity has been proposed.

Acknowledgements

This work was financially supported by the National Basic Research Program of China (973 Program, Nos. 2009CB939704, 2009CB939705), the National Natural Science Foundation of China (No. J1210061), Large-scale Instrument And Equipment Sharing Foundation of Wuhan University (No. LF20150582).

Appendix A. Supplementary data

Supplementary data associated with this article can be found, in the online version, at <http://dx.doi.org/10.1016/j.apcatb.2015.05.059>

References

- [1] M.N. Chong, B. Jin, C.W.K. Chow, C. Saint, *Water Res.* 44 (2010) 2997–3027.
- [2] A. Huang, N. Wang, M. Lei, L. Zhu, Y. Zhang, Z. Lin, D. Yin, H. Tang, *Environ. Sci. Technol.* 47 (2013) 518–525.
- [3] C. Pan, Y. Zhu, *Environ. Sci. Technol.* 44 (2010) 5570–5574.
- [4] G. Liu, L. Wang, H.G. Yang, H. Cheng, G.Q. Max Lu, *J. Mater. Chem.* 20 (2010) 831.
- [5] M.R. Hoffmann, S.T. Martin, W. Choi, D.W. Bahnemann, *Chem. Rev.* 95 (1995) 69–96.
- [6] A. Fujishima, T.N. Rao, D.A. Tryk, *J. Photochem. Photobiol. C* 1 (2000) 1–21.
- [7] A.L. Linsebigler, G.Q. Lu, J.T. Yates Jr., *Chem. Rev.* 95 (1995) 735–758.
- [8] Z.Y. Liu, D.D. Sun, P. Guo, J.O. Leckie, *Nano. Lett.* 7 (2007) 1081–1085.
- [9] Y. Lan, X.P. Gao, H.Y. Zhu, Z.F. Zheng, T.Y. Yan, F. Wu, S.P. Ringer, D.Y. Song, *Adv. Funct. Mater.* 15 (2005) 1310–1318.
- [10] S.P. Albu, A. Ghicov, J.M. Macak, R. Hahn, P. Schmuki, *Nano. Lett.* 7 (2007) 1286–1289.
- [11] Y. Takezawa, H. Imai, *Small* 2 (2006) 390–393.
- [12] B. Zhao, F. Chen, Q.W. Huang, J.L. Zhang, *Chem. Commun.* 34 (2009) 5115–5117.
- [13] D.V. Bavykin, A.N. Kulak, F.C. Walsh, *Cryst. Growth Des.* 10 (2010) 4421–4427.
- [14] U.I. Gaya, A.H. Abdullah, *J. Photochem. Photobiol. C* 9 (2008) 1–12.
- [15] W. Lee, Y. Sung, *Cryst. Growth Des.* 12 (2012) 5792–5795.
- [16] V.N. Kuznetsov, V.K. Ryabchuk, A.V. Emeline, R.V. Mikhaylov, A.V. Rudakova, N. Serpone, *Chem. Mater.* 25 (2013) 170–177.
- [17] H. Choi, Y.J. Kim, R.S. Varma, D.D. Dionysiou, *Chem. Mater.* 18 (2006) 5377–5384.
- [18] J. Yu, L. Qi, M. Jaroniec, *J. Phys. Chem. C* 114 (2010) 13118–13125.
- [19] B.D. Yao, Y.F. Chan, X.Y. Zhang, W.F. Zhang, *Appl. Phys. Lett.* 82 (2003) 281–283.
- [20] F. Chen, P. Fang, Y. Gao, Z. Liu, Y. Liu, Y. Dai, *Chem. Eng. J.* 204–206 (2012) 107–113.
- [21] F. Chen, P. Fang, Z. Liu, Y. Gao, Y. Liu, Y. Dai, H. Luo, J. Feng, *J. Mater. Sci.* 48 (2013) 5171–5179.
- [22] M. Pelaez, N.T. Nolan, S.C. Pillai, M.K. Seery, P. Falaras, A.G. Kontos, P.S.M. Dunlop, J.W.J. Hamilton, J.A. Byrne, K. O'Shea, M.H. Entezari, D.D. Dionysiou, *Appl. Catal. B* 125 (2012) 331–349.
- [23] K. Iketani, R. Sun, M. Toki, K. Hirota, O. Yamaguchi, *Mater. Sci. Eng. B* 108 (2004) 187–193.
- [24] J.C.S. Wu, C. Chen, *J. Photochem. Photobiol. A* 163 (2004) 509–515.
- [25] H. Yamashita, M. Harada, J. Misaka, M. Takeuchi, K. Ikeue, M. Anpo, *J. Photochem. Photobiol. A* 148 (2002) 257–261.
- [26] Y. Wang, R. Zhang, J. Li, L. Li, S. Lin, *Nanoscale Res. Lett.* 9 (2014) 46.
- [27] H. Peng, J. Li, S. Li, J. Xia, *J. Phys. Chem. Matter.* 20 (2008) 125207.
- [28] G. Shao, *J. Phys. Chem. C* 112 (2008) 18677–18685.
- [29] M.M. Mohamed, I. Othman, R.M. Mohamed, *J. Photochem. Photobiol. A* 191 (2007) 153–161.
- [30] J. Li, J. Chen, R. Ke, C. Luo, J. Hao, *Catal. Commun.* 8 (2007) 1896–1900.
- [31] M.S. Whittingham, *Curr. Opin. Solid State Mater. Sci.* 1 (1996) 227–232.
- [32] A. Di Paola, G. Marci, L. Palmisano, M. Schiavello, K. Uosaki, S. Ikeda, B. Ohtani, *J. Phys. Chem. B* 106 (2002) 637–645.
- [33] E. Hosono, H. Matsuda, I. Honma, M. Ichihara, H. Zhou, *Langmuir* 23 (2007) 7447–7450.
- [34] C. Tsai, H. Teng, *Chem. Mater.* 18 (2006) 367–373.
- [35] Y. Suzuki, S. Yoshikawa, *J. Mater. Res.* 19 (2004) 982–985.
- [36] K.S.W. Sing, *Pure Appl. Chem.* 57 (1985) 603–619.
- [37] Z. Chang, J. Liu, J. Liu, X. Sun, *J. Mater. Chem.* 21 (2010) 277–282.
- [38] E. Horváth, Á. Kukovecz, Z. Kónya, I. Kiricsi, *Chem. Mater.* 19 (2007) 927–931.
- [39] W. Su, J. Zhang, Z. Feng, T. Chen, P. Ying, C. Li, *J. Phys. Chem. C* 112 (2008) 7710–7716.
- [40] T. Ohsaka, F. Izumi, Y. Fujiki, *J. Raman Spectrosc.* 7 (1978) 321–324.
- [41] M. Wei, Y. Konishi, H. Arakawa, *J. Mater. Sci.* 42 (2007) 529–533.
- [42] W. Göpel, G. Rocker, R. Feierabend, *Phys. Rev. B* 28 (1983) 3427.
- [43] H. Xia, J. Feng, H. Wang, M.O. Lai, L. Lu, *J. Power Sources* 195 (2010) 4410–4413.
- [44] A. Moses Ezhil Raj, S.G. Victoria, V.B. Jothy, C. Ravidhas, J. Wollschläger, M. Suendorf, M. Neumann, M. Jayachandran, C. Sanjeeviraja, *Appl. Surf. Sci.* 256 (2010) 2920–2926.
- [45] J.G. Yu, X.J. Zhao, Q.N. Zhao, *Mater. Chem. Phys.* 69 (2001) 25–29.
- [46] A.B. Boffa, H.C. Galloway, P.W. Jacobs, J.J. Benítez, J.D. Batteas, M. Salmeron, A.T. Bell, G.A. Somorjai, *Surf. Sci.* 326 (1995) 80–92.
- [47] Y. Liu, P. Fang, Y. Cheng, Y. Gao, F. Chen, Z. Liu, Y. Dai, *Chem. Eng. J.* 219 (2013) 478–485.
- [48] C. Poinsignon, G. Berthome, B.N.D. Pre Lot, F. Thomas, F.D.R. Villie Ras, *J. Electrochem. Soc.* 151 (2004) A1611–A1616.
- [49] C.J. Cong, L. Liao, Q.Y. Liu, J.C. Li, K.L. Zhang, *Nanotechnology* 17 (2006) 1520–1526.
- [50] F. Alvarez-Ramirez, Y. Ruiz-Morales, *Chem. Mater.* 19 (2007) 2947–2959.
- [51] Y. Cong, J. Zhang, F. Chen, M. Anpo, D. He, *Preparation, J. Phys. Chem. C* 111 (2007) 10618–10623.
- [52] F. Chen, Z. Liu, Y. Liu, P. Fang, Y. Dai, *Chem. Eng. J.* 221 (2013) 283–291.
- [53] S. Asuha, X.G. Zhou, S. Zhao, *J. Hazard. Mater.* 181 (2010) 204–210.
- [54] K.I. Ishibashi, A. Fujishima, T. Watanabe, K. Hashimoto, *Electrochem. Commun.* 2 (2000) 207–210.
- [55] E. Szabó-Bárdos, K. Somogyi, N. Törő, G. Kiss, A. Horváth, *Appl. Catal. B* 101 (2011) 471–478.
- [56] S.D. Sharma, K.K. Saini, C. Kant, C.P. Sharma, S.C. Jain, *Appl. Catal. B* 84 (2008) 233–240.
- [57] T. Wang, W. Liu, L. Xiong, N. Xu, J. Ni, *Chem. Eng. J.* 215–216 (2013) 366–374.
- [58] W. Liu, J. Ni, X. Yin, *Water Res.* 53 (2014) 12–25.